Monthly Notices of the ROYAL ASTRONOMICAL SOCIETY

MNRAS **505,** 4422–4443 (2021)
Advance Access publication 2021 June 7

https://doi.org/10.1093/mnras/stab1611

The temperatures of red supergiants in low-metallicity environments

Gemma González-Torà,[1]★ Ben Davies,[1] Rolf-Peter Kudritzki[2,3] and Bertrand Plez[4]

[1]*Astrophysics Research Institute, Liverpool John Moores University, Liverpool Science Park IC2, 146 Brownlow Hill, Liverpool L3 5RF, UK*
[2]*LMU München, Universitäts-sternwarte, Scheinerst 1, D-81679 München, Germany*
[3]*Institute for Astronomy, University of Hawaii at Manoa, 2580 Woodlawn Drive, Honolulu, HI 96822, USA*
[4]*CNRS, LUPM, UMR 5299, Université de Montpellier, F-34095 Montpellier, France*

Accepted 2021 June 1. Received 2021 June 1; in original form 2021 February 9

ABSTRACT

The temperatures of red supergiants (RSGs) are expected to depend on metallicity (Z) in such a way that lower Z RSGs are warmer. In this work, we investigate the Z-dependence of the Hayashi limit by analysing RSGs in the low-Z galaxy Wolf–Lundmark–Mellote, and compare with the RSGs in the higher Z environments of the Small Magellanic Cloud and Large Magellanic Cloud. We determine the effective temperature ($T_{\rm eff}$) of each star by fitting their spectral energy distributions, as observed by VLT + SHOOTER, with MARCS model atmospheres. We find average temperatures of $T_{\rm eff_{WLM}} = 4400 \pm 202$ K, $T_{\rm eff_{SMC}} = 4130 \pm 103$ K, and $T_{\rm eff_{LMC}} = 4140 \pm 148$ K. From population synthesis analysis, we find that although the Geneva evolutionary models reproduce this trend qualitatively, the RSGs in these models are systematically too cool. We speculate that our results can be explained by the inapplicability of the standard solar mixing length to RSGs.

Key words: stars: atmospheres – stars: evolution – stars: fundamental parameters – stars: late-type – stars: massive.

1 INTRODUCTION

Red supergiants (RSGs) are an evolved state of massive stars. They have luminosities of $\sim 10^{4.39-5.52}$ L$_\odot$ (Davies & Beasor 2020), and comparing with evolutionary models (e.g. Georgy et al. 2013), a mass range of $\sim$ 8–25 M$_\odot$. The effective temperature ($T_{\rm eff}$) of RSGs is thought to be a manifestation of the Hayashi limit. The Hayashi limit (Hayashi & Hoshi 1961) fixes the minimum $T_{\rm eff}$ of the star and its maximum radius, where the star is known to have its most extended convective region and still maintaining hydrostatic equilibrium.

Theoretical predictions show a dependence of the average $T_{\rm eff}$ of RSGs on their metallicity (Z; see, for instance, the series Meynet & Maeder (2000, 2002) and Maeder & Meynet (2001), where stellar evolution in low metallicities has been extensively studied).

An explanation for the $Z - T_{\rm eff}$ dependence of RSGs from a physical point of view was proposed by Maeder & Meynet (2001): for lower Z, the star has a lower opacity and molecular weight. This will result in a more compact main-sequence star with a smaller, hotter convective core. At the end of the main sequence, the He-burning core has a shallower potential, which corresponds to a smaller and warmer RSG. The prediction can be tested by studying the average $T_{\rm eff}$ of RSGs in galaxies with different metallicities.

However, accurately measuring the $T_{\rm eff}$ of RSGs is known to be problematic. Specifically, Davies et al. (2013) showed that the $T_{\rm eff}$ obtained from model fits to the TiO bands (which is the most prominent spectral feature for these cool stars) were systematically cooler than fits of the same models to the line-free continuum of the spectral energy distribution (SED). An explanation for the different $T_{\rm eff}$ obtained when studying the TiO bands and the line-free continuum is provided by Davies et al. (2013). Broadly, the line-free regions in the spectrum form close to the photosphere, where the local temperature is close to the $T_{\rm eff}$. In contrast, the TiO bands can form much further out above the photosphere, where the temperature is $\sim$1000 K lower. To get consistent temperatures from both diagnostics, the model atmosphere used would have to be able to correctly predict the temperature structure from the photosphere out to many stellar radii. Davies et al. (2013) argued that 1D models provide a poor description of the outer temperature structure of RSGs. They suggested that models properly accounting for 3D radiative–hydrodynamics effects could yield consistent temperatures from both diagnostics. By adding a wind to the hydrostatic atmosphere, which increases the TiO absorption whilst leaving the rest of the optical–IR spectrum largely unchanged, a simultaneous fit to the TiO bands and the line-free continuum may be obtained (Davies & Plez, in preparation).

In this work, we use a $T_{\rm eff}$ determination method independent of the TiO bands, by fitting the whole of the SED except the regions dominated by the molecular and line absorption (as in Davies et al. 2013). We have analysed three samples of RSGs from the Local Group neighbouring galaxies Wolf–Lundmark–Mellote (WLM), Small Magellanic Cloud (SMC) and Large Magellanic Cloud (LMC), to investigate the Z-dependence of the average RSG $T_{\rm eff}$ across a broader baseline than was previously studied in Davies et al. (2013). The $T_{\rm eff}$ and extinctions ($A_{\rm V}$) have been obtained for WLM, SMC and LMC, as well as the bolometric luminosities ($L_{\rm bol}$) for WLM targets using synthetic and observed photometry. We also perform a population synthesis using the theoretical evolutionary tracks by Ekström et al. (2012), Georgy et al. (2013), and Groh et al. (2019), and compare the observations with the predictions from the simulations to better study the $T_{\rm eff}$ – [Z] dependence [where $[Z] = \log(Z/Z_\odot)$, with respect to solar $Z_\odot = 0.014$].

★ E-mail: g.gonzalezitora@2019.ljmu.ac.uk

This paper is organized as follows: Section 2 describes the observations and data reduction. The method used is presented in Section 3, followed by the results obtained in Section 4 and a discussion in Section 5, where we explore the implications of the determined temperatures and compare to simulations. Lastly, we conclude in Section 6.

2 OBSERVATIONS AND DATA REDUCTION

2.1 New data

We have observed several RSGs in WLM, selecting our targets from Levesque & Massey (2012). We chose the nine brightest objects in the near-IR (NIR), which represents all RSGs in this galaxy with luminosities $\log(L_{\rm bol}/L_{\odot}) > 4.4$ (see Fig. 3). Our targets are listed in Table 3. We observed each star with VLT + XSHOOTER (D'Odorico et al. 2006) in order to obtain contemporaneous spectrophotometry from the optical to the NIR, under the ESO program number [093.D-0021(A), PI: B Davies]. All stars were observed with the 5 arcsec slit to minimize slit losses, in an ABBA nodding pattern. Slit positions were defined specifically to avoid any nearby stars clashing in the dispersion direction. The total integration times were the same for each star; 2248, 2760, and 3040 s in the UVB, VIS, and NIR arms, respectively. The NIR integrations were broken up into discrete integration times of 190 s to avoid saturation in the airglow emission lines. In addition to the science targets, telluric standard stars of spectral type B were observed within 1.5 h of any science exposure. Data were reduced following the same procedure described in Davies et al. (2013).

When observing the stars from a very distant galaxy such as WLM, we cannot rule out the possibility that the RSGs observed are part of multiple systems, and other stars can contribute to the flux measured. However, at the resolution of ground-based survey imaging, we see no evidence of source confusion from abnormal colours or point spread functions. In addition, we see no evidence of hybrid spectral features (e.g. Balmer lines) in the blue, which would be indicative of an unresolved multiple system. Even with other targets being in the slit, RSGs are much brighter than anything else so the likelihood of significant contamination is small.

While performing the analysis, we found that the WLM star number 7 (WLM 07) in Table 3 has a radial velocity $v = 30\,{\rm km\,s^{-1}}$, while all the others are $v \sim 120\,{\rm km\,s^{-1}}$. Checking their parallaxes at SIMBAD (Wenger et al. 2000), WLM 07 has 1.4307 ± 0.6966 mas (Gaia Collaboration 2018), while the other targets have parallaxes consistent with 0 mas (Gaia Collaboration 2018). Both velocities and parallaxes of WLM 07 are not coincident with the rest of the WLM targets in within the errors. Furthermore, this star has a spectral type (M3) which is much later than the others (K0-3, see Table 3). We have assumed that the target is a foreground star and not part of WLM. For these reasons, WLM 07 has been excluded from further analysis.

2.2 Archival data

For the LMC and SMC, we used the previous data from the VLT + XSHOOTER observations, under the ESO programme number 088.B-0014(A) (PI B. Davies). The observations, selection criteria, and reduction steps are described in Davies et al. (2013, 2015). The stars from LMC and SMC were selected from Levesque et al. (2006) to sample the full distribution of spectral types in each galaxy (as explained in Davies et al. 2013). As a further test that our sub-sample of stars in each galaxy has a distribution of $T_{\rm eff}$ representative of the entire RSG population of that galaxy, we perform the following tests: we randomly select 10 RSGs from Tabernero et al. (2018) that have the same spectral type distribution as our sample stars. For each of these 10 stars, we randomly assign a $T_{\rm eff}$ based on that star $T_{\rm eff}$ measurement and associated error in Tabernero et al. (2018). Next, we obtain the average $T_{\rm eff}$ of these 10 randomly selected temperatures. We repeat this process 100 times for both LMC and SMC targets. Finally, we compare the results with the average $T_{\rm eff}$ of the whole sample in Tabernero et al. (2018). The error in the average temperatures is calculated with the mean error of the individual stars and the standard deviation.

Table 1. Results of the statistical significance test. The left column indicates the galaxy studied, the middle column shows the average $T_{\rm eff}$ retrieved given our sub-sample from Tabernero et al. (2018), the right column shows the average $T_{\rm eff}$ for the full sample in Tabernero et al. (2018).

Galaxy	Sub-sample $\overline{T}_{\rm eff}$ (K)	Full sample $\overline{T}_{\rm eff}$ (K)
LMC	3800 ± 50	3810 ± 100
SMC	3940 ± 30	3970 ± 70

Checking the results in Table 1, we see that the mean value for the sub-sample distribution is within the error limits of the average temperature of the whole RSGs sample in Tabernero et al. (2018). Both results are coincident within the error limits. Therefore, we conclude that our two sub-samples of stars have $T_{\rm eff}$ distributions consistent with those of the entire population in each galaxy.

3 DETERMINATION OF EFFECTIVE TEMPERATURES

We begin with a grid of model atmospheres generated with the MARCS code (Gustafsson et al. 2008). The 1D code assumes local thermodynamic equilibrium (LTE), hydrostatic equilibrium, and spherical symmetry. We fixed the metallicities to be $[Z]_{\rm WLM} = -1.0$ (Urbaneja et al. 2008), $[Z]_{\rm LMC} = -0.35$, and $[Z]_{\rm SMC} = -0.55$ (Davies et al. 2015). As for the metallicity adopted in WLM, in Urbaneja et al. (2008) it is stated that previous photometric studies show WLM as having a young population in the disc, and an old metal-poor halo. By observing the red giant branch colour, McConnachie et al. (2005) found a metallicity of $[Z] = -1.45$ with respect to solar. This result, however, did not take into account the contribution of the younger population. When inspecting rich-metal line spectra of A supergiants, Urbaneja et al. (2008) found an average metallicity of $[Z] = -0.87 \pm 0.06$. The $[Z]_{\rm WLM} = -1.0$ adopted in this work is consistent with that found from analysis of WLM blue supergiants by Urbaneja et al. (2008) once the differences in the solar abundances used in that study and ours are taken into account (see appendix of Davies et al. 2017).

We assumed the fiducial values for the microturbulence of $\xi = 3\,{\rm kms^{-1}}$ (see Davies et al. 2015). Surface gravities used are $\log g = -0.2$ for the Magellanic Clouds (MCs), as in Davies et al. (2015), while for WLM $\log g = 0$. The $\log g$ of the WLM stars was found iteratively, by comparing their luminosities and temperatures determined from our analysis with the evolutionary tracks of Georgy et al. (2013). We have found gravities ranging from -0.2 to $+0.4$, with the majority around $\sim$0.0. The robustness of our results to these fiducial values for gravity, metallicity, and microturbulence are discussed in Section 4.1. The model grid is computed between $3400\,{\rm K} < T_{\rm eff} < 5000\,{\rm K}$ in steps of 100 K, which we then interpolate into a finer grid of 20 K steps.

Table 2. Regions used of the SED for the analysis.

λ_{min} (nm)	λ_{max} (nm)
821.6	831.9
871.7	880.0
1036	1080
1212	1278
1610	1614
1649	1659
1716	1723
2120	2250

In addition to fitting for the best $T_{\rm eff}$, we also allow the extinction $A_{\rm V}$ to vary, since this parameter can make the star appear cooler and create a large degree of degeneracy with $T_{\rm eff}$. For the MCs, we use the extinction law of Gordon et al. (2003), which is specifically tuned to the interstellar medium in the direction of these galaxies. For WLM, we use instead the law derived by Cardelli, Clayton & Mathis (1989), and assume a $R_{\rm V} = 3.1$ as of the Milky Way. The robustness of this assumption is explored in Section 4.1. For the baseline (i.e. Galactic) extinction towards WLM, Schlafly et al. (2014) shows that it is very low, and consistent with zero [$0 \leq E(B-V) \leq 0.1$]. Therefore, it will not influence our results. The grid of extinction parameters used is $0 < A_{\rm V} < 2$ with a step of 0.01.

For the analysis, we fit the SED windows unaffected by line and molecular absorption as seen in Table 2, which are the same used in Davies et al. (2013). We avoid the *BVR* spectral region, the molecular absorption bands of TiO, VO, CO (at $\sim$ 1.5 μm and $>$ 2.3 μm), and the CN band at 1.1 μ m. While Davies et al. (2013) performed a pixel-by-pixel matching of these spectral regions, we fit the mean flux of each SED window. The reason is that the signal-to-noise ratio (SNR) in the NIR region of the WLM spectra are not high enough to do pixel-by-pixel analysis.

At each point in the model grid (i.e. for each value of $T_{\rm eff}$ and $A_{\rm V}$), we adjusted the SED to the same data flux by minimising the $\sum(\log(SED_{\rm model}) - \log(SED_{\rm data}))$ at the line-free continuum, where $\log(SED)$ represents the base-10 logarithm of the SED flux regions, in order to compare both fluxes. We then performed a 2-parameter fit by means of a χ^2 minimization, assuming Gaussian correlation as shown in equation (1):

$$\chi_i^2 = \sum_{i=1}^{n} \frac{(SED_{\rm data} - SED_{\rm model})_i^2}{\sigma_i^2}, \quad (1)$$

where n is the number of spectral regions in Table 2, $SED_{\rm data}$ represents the mean flux of the data for each one of the regions, $SED_{\rm model}$ the mean flux of the model, and σ_i^2 the standard deviation of the data in each SED region.

The result of the analysis is a 2D-array of χ^2, one value for each $A_{\rm V}$ and $T_{\rm eff}$. The best-fitting parameters correspond to those at the minimum value of the χ^2 2D-array.

For the errors on $T_{\rm eff}$ and $A_{\rm V}$, we first determine the 68 per cent dispersion contours of the χ^2 fit that for 2 degrees of freedom like the present case ($T_{\rm eff}$ and $A_{\rm V}$) corresponds to all the grid models with values $\chi^2 < \chi^2_{\rm min} + 2.3$ (Avni 1976), where $\chi^2_{\rm min}$ is the best-fitting model. The errors on each parameter are then defined as being the minimum values within this range.

The $L_{\rm bol}$ were calculated for WLM targets using synthetic photometry and available photometry at the SIMBAD data base (Wenger et al. 2000), with 2MASS (Pickles & Depagne 2010), *Gaia* DR2 (Gaia Collaboration 2018), PAN-STARSS (Chambers et al. 2016), VISTA (McMahon et al. 2013), SkyMapper (Wolf et al. 2018), and *Spitzer*/IRAC (Boyer et al. 2015) photometry. The magnitudes for the different filters were converted to flux, dereddened using the previously determined extinction $A_{\rm V}$, and integrated over the wavelength range for all the photometric filters available (from 0.36 to 7.5 μm). We transformed to bolometric luminosities using the most recent distance determination $d_{\rm WLM} = 995 \pm 46$ kpc (Urbaneja et al. 2008). Dorda et al. (2016) showed that SMC RSGs display a high degree of spectral variability, finding evidence that variability increases with decreasing metallicity. Furthermore, Beasor et al. (2021) studied the effect of the variability between the minimum and maximum states of the RSGs in the stellar cluster Westerlund 1. Even when the most extreme assumptions were made, the resulting impact on the $L_{\rm bol}$ was at most ±0.2 dex. Therefore, any systematic uncertainty due to spectral variability in the stars in this work must be less than this.

To determine the error on $L_{\rm bol}$, we propagated the errors through those on the individual flux measurements, the error on $A_{\rm V}$, as well as the distance of the galaxy. Of these, the dominant source of uncertainty is the $A_{\rm V}$.

4 RESULTS

The best $T_{\rm eff}$, $A_{\rm V}$, and $\log(L_{\rm bol}/L_{\odot})$ obtained after the analysis, for each object in WLM is listed in Table 3 (with the errors from the 68 per cent $\Delta\chi^2$ isocontours), as well as their stellar coordinates, apparent magnitudes, spectral types from Levesque & Massey (2012), and identification names as in the SIMBAD data base (Wenger et al. 2000). Fig. 1 shows the results of the analysis for one case, where we see the best-fitting MARCS model (upper left-hand panel) in black with respect to the data in red, the residuals of the fit in the lower left-hand panel. The right-hand panel of Fig. 1 shows the best-fitting parameters along with the ellipse dispersion contours for the 68 per cent, 95 per cent, and 99.7 per cent confidence limits. The best fits for the rest of the targets can be seen in Figures A1–A28 of Appendix A.

In Appendix A, we see that for WLM 01, 05, and 09 there is a continuum shift for the long-wavelength edge in the observations. This is because in the last order of the NIR arm there was a variable thermal background that affected the flux calibration. To investigate the impact of this effect, we repeated the analysis shifting the fitted region at this order for these particular cases. The results did not change for the first 2 cases, and changed by −20 K in WLM 09. This does not increase the errors for these stars. Moreover, WLM 01 has an extinction close to zero of $A_{\rm v} = 0.00 \pm 1.02$, but one of the biggest error budgets of all WLM stars.

Table 4 shows the calculated values with the SED method for the SMC and LMC stars, with the errors in $T_{\rm eff}$ and $A_{\rm V}$ from the 68 per cent $\Delta\chi^2$ isocontours. We have compared the stars with the previous results from Davies et al. (2013, 2015), and Tabernero et al. (2018) in Fig. 2. The results are consistent between 1σ and 2σ for the first two panels; the discrepancy with Tabernero et al. (2018) is discussed in Section 4.2.

There is one particular case in LMC that needs to be taken with care. Checking Fig. A24, we see that for LMC 136042 the observations (upper left-hand panel, in blue) tend to upper the continuum in the spectral region of <500 nm, meaning that their flux contribution at the green–blue region of the spectra is higher than expected. This indicates that there is a blue star next to this target (González-Fernández et al. 2015). We excluded this target for the rest of the analysis.

Table 3. Table shows the ID name, RA, Dec., m_R (in magnitudes), spectral type as indicated at the SIMBAD data base, and the best T_{eff}, A_V, and $\log(L_{bol}/L_\odot)$ obtained for each studied RSG at the WLM galaxy, within their 68 per cent confidence limits. WLM 07 is suspected to be a foreground star.

Star	ID	RA	Dec.	m_R	T_{eff} (K)	A_V	$\log(L_{bol}/L_\odot)$	SpT
WLM 01	LGGS J000153.17-152813.4	00 01 53.181	−15 28 13.92	18.51	4580^{+420}_{-180}	$0.00^{+1.02}$	$4.47^{+0.08}_{-0.12}$	K0-1I
WLM 02	LGGS J000156.77-152839.6	00 01 56.785	−15 28 40.18	16.62	4660^{+340}_{-440}	$0.95^{+0.54}_{-0.95}$	$5.52^{+0.07}_{-0.06}$	K2-3I
WLM 03	LGGS J000156.87-153122.3	00 01 56.887	−15 31 22.84	17.91	4220^{+220}_{-120}	$0.08^{+0.54}_{-0.08}$	$4.80^{+0.11}_{-0.05}$	K0-1I
WLM 04	LGGS J000157.01-152954.0	00 01 57.023	−15 29 54.59	17.85	4560^{+440}_{-360}	$0.65^{+0.84}_{-0.65}$	$4.89^{+0.09}_{-0.07}$	K0-1I
WLM 05	LGGS J000157.55-152915.8	00 01 57.545	−15 29 16.05	18.41	4160^{+780}_{-140}	$0.11^{+1.38}_{-0.11}$	$4.66^{+0.13}_{-0.06}$	K0-1I
WLM 07	LGGS J000158.14-152332.2	00 01 58.146	−15 23 32.58	18.62	4460^{+540}_{-140}	$0.00^{+1.15}_{-0.01}$	$4.48^{+0.09}_{-0.04}$	M3I
WLM 08	LGGS J000158.74-152245.5	00 01 58.746	−15 22 46.03	17.56	4420^{+560}_{-220}	$0.40^{+1.04}_{-0.40}$	$4.98^{+0.07}_{-0.06}$	K0-1I
WLM 09	LGGS J000200.81-153115.7	00 01 59.610	−15 30 59.90	18.07	4340^{+160}_{-160}	$0.34^{+0.41}_{-0.34}$	$4.80^{+0.08}_{-0.07}$	K2-3I
WLM 10	LGGS J000200.81-153115.7	00 02 00.810	−15 31 15.70	17.78	4380^{+200}_{-220}	$0.60^{+0.51}_{-0.57}$	$4.84^{+0.10}_{-0.06}$	K0-1I

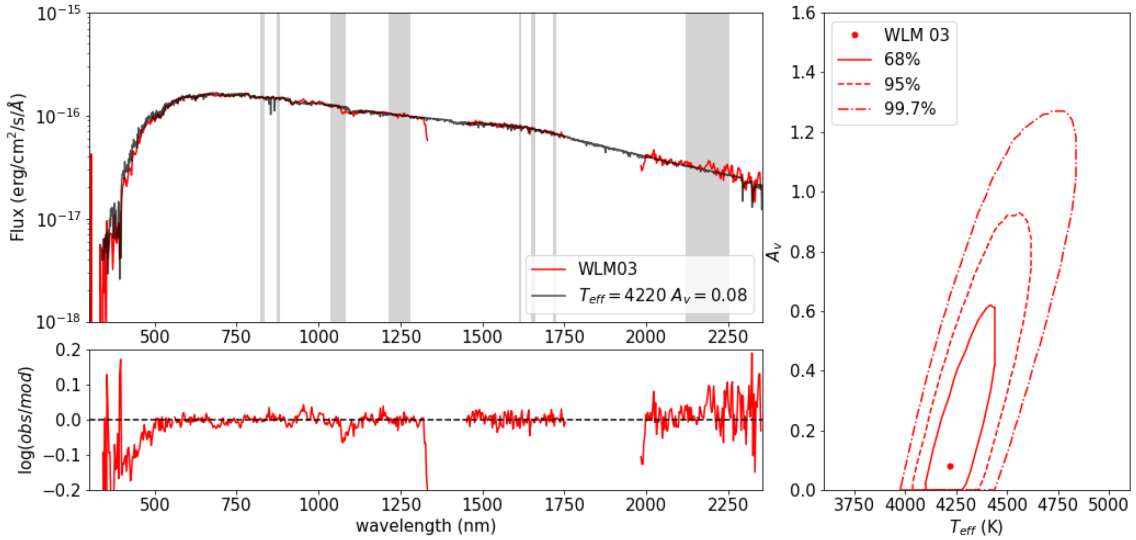

Figure 1. Three panels showing the results of the analysis. *Upper left:* Shows the smoothed data (red) and best fitted MARCS model (black), while the SED regions for the analysis are shown in grey. *Lower left:* The residuals of the fit. *Right:* shows the 68 per cent, 95 per cent, and 99.7 per cent confidence limits for the best-fitting T_{eff} and A_V.

The stars are placed in the Hertzprung–Russel diagram (HRD) in Fig. 3, based on their L_{bol} and T_{eff}. We have also plotted for comparison the 9–20 $M_\odot$ rotating evolutionary tracks for RSGs taken from Georgy et al. (2013), in the black solid line showing the tracks corresponding to a $Z = 0.002$, comparable to the studied galaxies. The average values for the three galaxies (excluding WLM 07 and LMC 136042, for the reasons already mentioned), are

WLM: $T_{eff} = 4400 \pm 202$ K,

SMC: $T_{eff} = 4130 \pm 103$ K,

LMC: $T_{eff} = 4140 \pm 148$ K,

where the errors correspond to the quadratic sum of the formal errors from the model fitting and the systematic errors arising from our assumptions when fitting the data (see Section 4.1).

With the results above we see that, as theory predicts (e.g. Maeder & Meynet 2001) there is a dependence with average T_{eff} of RSGs on Z for WLM and the MCs. Indeed, the lowest Z galaxy shows an average temperature ∼250 K higher than the MCs. In the case of the MCs, we are not able to resolve a temperature difference between these two galaxies. This result agrees with previous work from Davies et al. (2015), which claimed that there is no measurable dependence of T_{eff} on Z between the metallicities of LMC and SMC. In this work, we extend the metallicity baseline down to $[Z] = -1$, after which a trend on T_{eff} with Z becomes clear (see Fig. 6).

4.1 Robustness of the analysis

As described in Section 3, we made several assumptions in our fitting methodology. In this section, we now investigate the sensitivity of our results to these assumptions.

4.1.1 Microturbulence

To investigate the effect of varying our choice of ξ for the models employed, we repeated the analysis for each target with $\xi = 2$ and 4 km s^{-1} since Davies et al. (2015) found a range of ξ between 2 and 4 km s^{-1} for all MCs stars. The median T_{eff} does not change for WLM when assuming these ξ values, while for the MCs it changes in both by −10 K with $\xi = 2$, and +20 K for $\xi = 4$. We see that the

Table 4. Best $T_{\rm eff}$ and $A_{\rm V}$ obtained for each studied RSG at the SMC and LMC galaxies, within their 68 per cent confidence limits. The stars names are based on the catalogue available by Davies, Crowther & Beasor (2018).

Star	$T_{\rm eff}$ (K)	$A_{\rm V}$
SMC 011709	4100^{+120}_{-80}	$0.49^{+0.35}_{-0.3}$
SMC 013740	4040^{+100}_{-80}	$0.81^{+0.32}_{-0.32}$
SMC 020133	4160^{+120}_{-100}	$1.27^{+0.37}_{-0.39}$
SMC 021362	3940^{+80}_{-100}	$0.37^{+0.33}_{-0.35}$
SMC 030616	4140^{+100}_{-120}	$0.73^{+0.35}_{-0.39}$
SMC 034158	4180^{+80}_{-100}	$0.55^{+0.32}_{-0.37}$
SMC 035445	4120^{+100}_{-80}	$0.46^{+0.29}_{-0.28}$
SMC 049478	4180^{+100}_{-100}	$0.75^{+0.34}_{-0.37}$
SMC 050840	4000^{+100}_{-100}	$0.55^{+0.33}_{-0.36}$
SMC 057386	4160^{+160}_{-120}	$0.39^{+0.44}_{-0.38}$
LMC 064048	3880^{+140}_{-120}	$0.52^{+0.61}_{-0.52}$
LMC 067982	4140^{+140}_{-140}	$1.52^{+0.47}_{-0.60}$
LMC 116895	4140^{+160}_{-140}	$1.10^{+0.65}_{-0.56}$
LMC 131735	4280^{+120}_{-120}	$0.81^{+0.50}_{-0.44}$
LMC 136042	4100^{+100}_{-100}	$1.99^{+0.01}_{-0.30}$
LMC 137818	4040^{+160}_{-140}	$0.85^{+0.53}_{-0.55}$
LMC 142202	4160^{+100}_{-160}	$1.79^{+0.20}_{-0.66}$
LMC 143877	4300^{+100}_{-120}	$1.22^{+0.47}_{-0.45}$
LMC 158317	4140^{+120}_{-120}	$1.55^{+0.44}_{-0.54}$

effect of varying ξ is a factor of 10 smaller than the fitting errors. Therefore, a systematically different ξ in WLM cannot explain the $T_{\rm eff}$ differences between this galaxy and the MCs.

In short, the choice of ξ makes little to no difference to our results. The reason is that ξ will affect the strong absorption lines of the spectra, but in this work we are studying the line-free continuum.

4.1.2 Surface gravity

We also perform the analysis with log g $= -0.5$ and log g $= +0.5$ based on the gravity range found in Davies et al. (2015). We find that for log g $= -0.5$ in WLM the average temperature varies by -100 K while for the MCs it varies by -40 K for both. With log g $= +0.5$ the variation is $+80$ K for WLM, $+30$ K for SMC, and $+40$ K for LMC. As a consequence, we see that the choice of surface gravity seems to make an impact on the final results in WLM, while for the MCs the variation is again smaller. As commented in Section 3, we expect the range on surface gravities to be $-0.2 <$ log g $< +0.4$, with the majority around 0. This is comparable with the results from Davies et al. (2015).

To sum up, there is a stronger degeneracy when studying the effect of log g. This offset seems to be of ± 80 K, but cannot explain why the $T_{\rm eff}$ in WLM is $\sim$250 K higher than the MCs.

4.1.3 Extinction law

To check the robustness of the extinction law for WLM, we have performed the analysis using various values of $R_{\rm V}$ from 2 to 6. The results changed by less than 30 K for $R_{\rm V} = 2$, 4 and 5, while for a extreme assumption such as $R_{\rm V} = 6$ the difference was of only $+50$ K. Since WLM is a metal-poor environment, we also studied the effect of using a SMC-like extinction law, and found a difference on the average temperature of -20 K, all between the error limits. The best fit for $A_{\rm V}$ changes a maximum of $+0.09$ for the extreme assumption of $R_{\rm V} = 6$, and it is within the error limits for $A_{\rm V}$.

In conclusion, the choice of $R_{\rm v}$ and extinction law makes barely any difference when determining the $T_{\rm eff}$.

4.1.4 SED continuum regions

The last assumption that needs to be checked is the choice of the SED continuum regions. We have recalculated our results with slightly different SED regions (e.g. including a continuum region at $\sim$400 nm, or varying the *JHK* band regions in Table 2 by $\sim$50 nm). We find that the choice of continuum windows can shift the median $T_{\rm eff}$ in each galaxy by ± 60 K. We interpret this error to represent the absolute level of accuracy on our results. In other words, a median $T_{\rm eff}$ difference between two galaxies within 60 K would be consistent with zero.

Lastly, the choice of the SED continuum regions give a systematics of $\sim$60 K, this is smaller than the limitations obtained by the 68 per cent dispersion contours, and can be related with the accuracy of the method.

4.2 Comparison with previous studies

Davies et al. (2013) used two different methods to calculate the $T_{\rm eff}$ of the same targets: the first one has been conventionally used to analyse M-K-type stars, and is based on fitting the TiO spectral bands (between 500 and 800 nm). The second method is the same SED continuum fit as used for this work, but with a $\xi = 2\,{\rm km\,s^{-1}}$.[1] In the left-hand panel of Fig. 2 we compare our results to those of Davies et al. (2013). We notice that the star-to-star differences with Davies et al. (2013) are always in between 1σ for both MCs, and there is no systematic offset. The very slight discrepancies between the results from this work (*y*-axis) and Davies et al. (2013; *x*-axis) can be justified by the change in log g and ξ, as seen in Section 4.1.

In Davies et al. (2015), the method consists of comparing the strengths of different spectral lines on the *J* band with non-LTE model grids. We have used the same log g and ξ as in Davies et al. (2015). In the centre panel of Fig. 2, we can see that the results are consistent between 2σ, and obtain a median offset of $\sim$60 K, which is within the level of precision obtained by the choice of SED regions in Section 4.1. Despite the two completely different methodologies employed, the agreement is excellent.

The work of Tabernero et al. (2018) differs the most from this work (right-hand panel in Fig. 2). We have calculated a median offset of $\sim$150 K between both results, ours being warmer. In Tabernero et al. (2018), temperatures are estimated by fitting spectral lines in the *I* band with predictions from MARCS model atmospheres and LTE line formation.

The differences between our results and those of Tabernero et al. (2018) are twofold. Firstly, these LTE models do not include the non-LTE correction employed in Davies et al. (2015). This can account for $\sim$50 K (see Bergemann et al. 2013), assuming that the corrections in the I-band are similar to those in the *J* band.

Secondly, the region studied in Tabernero et al. (2018) of the I-band overlaps with a TiO absorption band. Davies et al. (2013) showed that the MARCS models cannot simultaneously reproduce the TiO bands and the continuum (see Figure set 1 in Levesque et al. 2005 and Figure set 2 in Levesque et al. 2006). This makes continuum

[1] As the Davies et al. (2013) study pre-dated the detailed spectral fitting in Davies et al. (2015) in which the microturbulent velocities were measured.

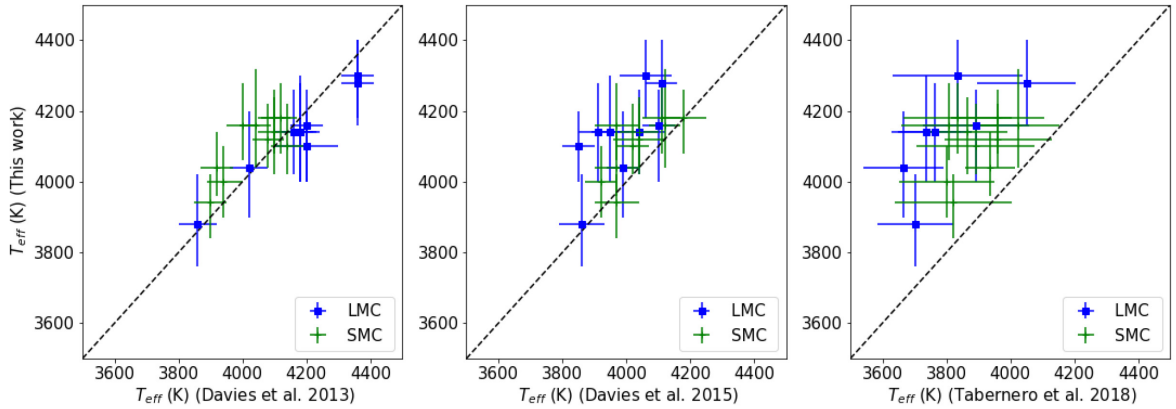

Figure 2. Comparison between the results from this work (*y*-axis) and the previous results found by Davies et al. (2013) (*left-hand panel*), Davies et al. (2015) (*centre panel*), and Tabernero et al. (2018) (*right-hand panel*). The SMC targets are represented in green, while the LMC in the blue squares. The black-dashed line shows the 1:1 ratio.

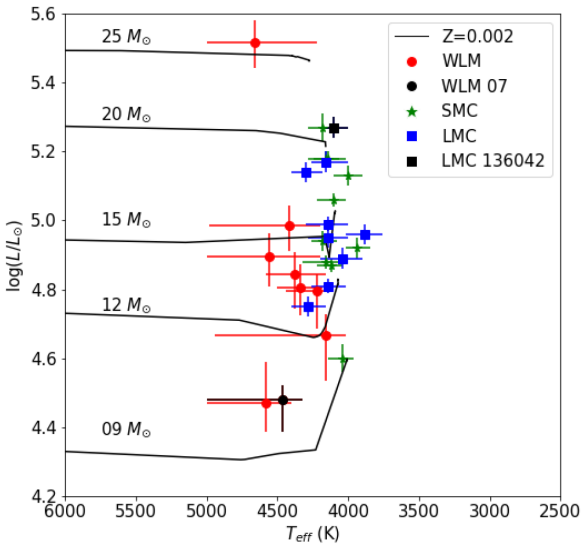

Figure 3. HRD showing the RSGs of WLM (red), LMC (blue), SMC (green), with the evolutionary tracks from Georgy et al. (2013), with a $Z = 0.002$, and rotation $v/v_c = 0.4$ comparable to the galaxies studied. The black dots correspond to the problematic targets. The luminosities for the MCs are taken from Davies et al. (2018).

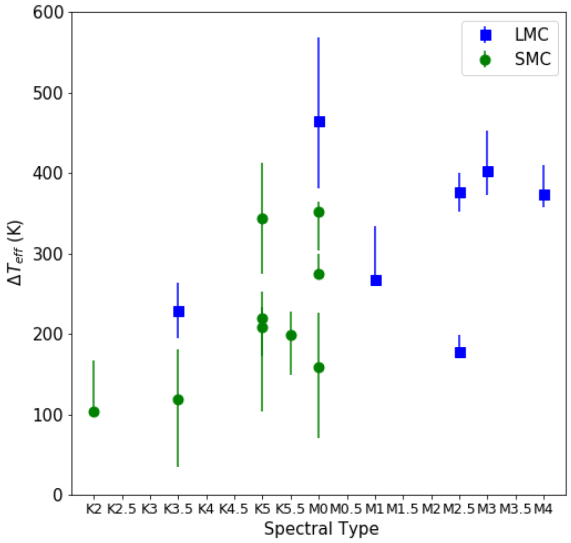

Figure 4. Panel showing the difference between the $T_{\rm eff}$ results from this work and Tabernero et al. (2018), with respect to the spectral type of each RSG studied in the LMC (the green dots) and the SMC (the blue squares), as in the SIMBAD data base.

placement in the *I* band gradually more problematic at spectral types M0 and later, as the contamination by TiO grows. Therefore, we would expect to see a trend of increasing disparity between the $T_{\rm eff}$ of Tabernero et al. (2018) and those of our study with increasing spectral type. Indeed, this is what we see in Fig. 4, a trend for the increasing difference between the $T_{\rm eff}$ of Tabernero et al. (2018) and those of our work ($\Delta T_{\rm eff}$) as we go to later spectral types, for both LMC and SMC. Therefore, we conclude that the systematic offset in Fig. 2 can at least be partially explained by this trend.

5 DISCUSSION

In Section 4, we have found an average $T_{\rm eff}$ of RSGs in WLM warmer than for the higher Z environments of the MCs. As seen in Section 4.1, these differences cannot be explained by systematics in the fitting method. In this section, we investigate how our results compare to the expectations from stellar evolution models.

To better understand how our results compare to model predictions, we performed a population synthesis analysis. We generated a number of simulated stars ($\sim 10^5$) with masses of 5–100 $M_\odot$ according to a Salpeter initial mass function. Then we assigned random ages, and used the evolutionary tracks of Ekström et al. (2012), Georgy et al. (2013), and Groh et al. (2019) to interpolate their luminosities and $T_{\rm eff}$ at that age. We disregarded stars that are not in the RSG phase or are older than their expected lifetime. We have then selected the stars with $4.4 < \log(L_{\rm bol}/L_\odot) < 5.6$ (following Davies & Beasor 2020) and $3000 < T_{\rm eff} < 5000$ K, corresponding to a RSG phase and the stars in our sample. We determine the $T_{\rm eff}$ distribution of the stars in the RSG phase. Fig. 5 shows the histograms of the $T_{\rm eff}$ from the RSGs after the population synthesis, for the case of non-rotating simulated stars with Z = 0.014, 0.002, and 0.0004. As expected, we see that for higher metallicities there is a trend to lower temperatures. This trend does not change if we use a $\log(L_{\rm bol}/L_\odot) = 4.5$ or 5 cut instead.

A clearer visualization of this Z dependence with $T_{\rm eff}$ can be seen in Fig. 6: the median $T_{\rm eff}$ of the simulated stars is shown with respect

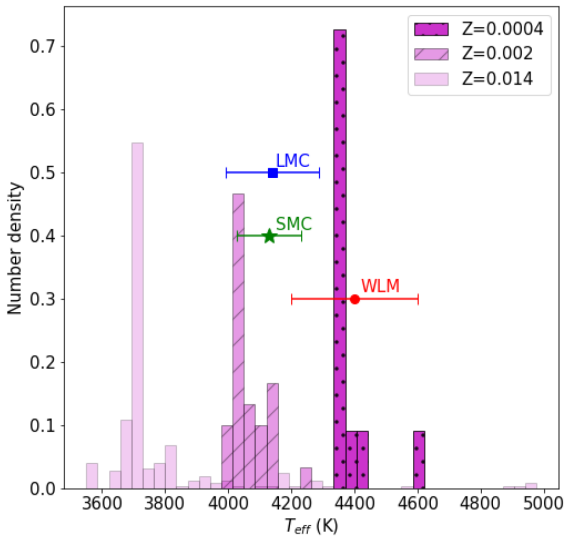

Figure 5. Histograms showing the number density of simulated stars, in solid magenta bins for Z = 0.014, dashed bins for Z = 0.002 and spotted bins for Z = 0.0004. The median temperature and error bars calculated with the observations for the three galaxies is also shown in green (SMC), blue (LMC), and red (WLM). The simulations shown are obtained for non-rotating stars.

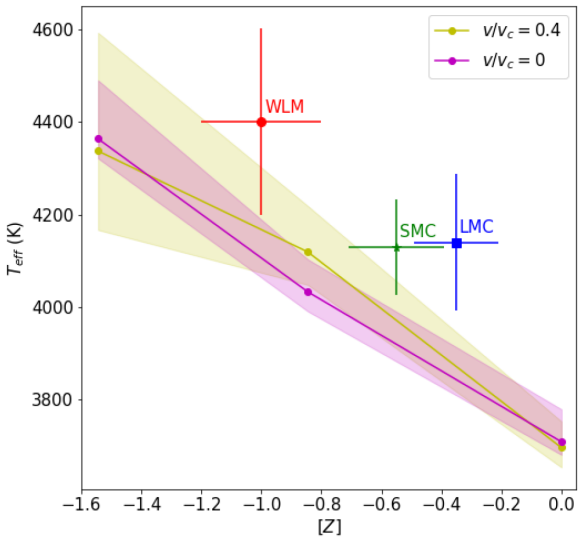

Figure 6. Plot showing the temperature trend with respect to the metallicity [Z], in yellow for rotating simulated stars, and magenta for non-rotating. The error limits in the trend are calculated using the 68 per cent dispersion of the cumulative distribution for the skewed histograms. The median temperatures and error bars calculated with the observations for the three galaxies are also shown in green (SMC), blue (LMC), and red (WLM).

to their [Z], in magenta for non-rotating and in yellow for rotating simulated stars. The shaded regions show the 68 per cent confidence limits (analogous to a 1σ standard deviation). The median $T_{\rm eff}$ are also shown in Fig. 6 for the observations of each galaxy. Comparing the model predictions with the data, we point out the following:

(i) For all three galaxies, the RSGs appear to be warmer than the model predictions.

(ii) The results show a similar qualitative slope in comparison with the simulations, but the models seem to be too cool, especially for the non-rotating models. This systematic offset is $\Delta T_{\rm eff_{WLM}} = 220$ K, $\Delta T_{\rm eff_{SMC}} = 140$ K, and $\Delta T_{\rm eff_{LMC}} = 250$ K for rotating models, while $\Delta T_{\rm eff_{WLM}} = 300$ K, $\Delta T_{\rm eff_{SMC}} = 220$ K, and $\Delta T_{\rm eff_{LMC}} = 300$ K for non-rotating. The offset is also out of the error dispersion for the LMC. The significance of this offset is discussed below.

To determine the statistical significance of the offset of the observed $T_{\rm eff}$ with respect to the model predictions, we perform a Monte Carlo (MC) test. Each MC trial is constructed as follows: first, for each galaxy, we randomly select N stars, where N is the number of stars observed in that galaxy (e.g. $N = 10$ in SMC). We note an individual star may be selected more than once per trial. Then, for each randomly selected star, we randomly assign a $T_{\rm eff}$ from that star's observed probability distribution (illustrated by, e.g. the right-hand panel in Fig. 1). Finally, we determine the median $T_{\rm eff}$, $\overline{T}_{\rm eff}$, of the N stars. We then repeat this process 1000 times to determine the probability distribution on $\overline{T}_{\rm eff}$ for each galaxy.

Using Fig. 6, we interpolate the simulated $T_{\rm eff}$ and its uncertainty at the metallicity of the galaxy, and its corresponding error limits. Next, we calculate the probability that the model fits the data by integrating the product of the observed and simulated $T_{\rm eff}$ distributions. We repeat this process for every galaxy.

For rotating models, we find a probability that the model and data agree of $p_{\rm WLM} = 0.07$, $p_{\rm SMC} = 0.03$, and $p_{\rm LMC} = 0.01$. The probability that all three galaxies are consistent with the rotating model predictions is $p_{\rm total} = 10^{-5}$. For non-rotating models we find $p_{\rm WLM} = 0.003$, $p_{\rm SMC} = 0.003$, $p_{\rm LMC} = 0.0004$, and $p_{\rm total} = 10^{-7}$. We conclude that the systematic offset between observed and predicted $T_{\rm eff}$ in all galaxies in this study cannot be explained by random scattering within the experimental errors.

A possible explanation to this mismatch between observations and simulations could be a breakdown in the assumptions used to simulate convection in RSGs. In 1D models, the mixing length theory (Böhm-Vitense 1958) is the analytic approximation used to describe the 3D phenomenon of convection. It assumes that a fluid parcel can travel a distance fixed by the so-called mixing length, l, before dispersing into the surrounding material. This mixing length is usually expressed in terms of the pressure scale height, $\alpha_{\rm MLT} = l/H_P$, where $\alpha_{\rm MLT}$ is the mixing length parameter. This free parameter is usually calibrated using the standard solar model with a single depth-independent $\alpha^{\odot}_{\rm MLT}$. This solar calibrated value is used for stars of all masses, metallicities, and evolutionary phases. Indeed, the evolutionary tracks in this work by Ekström et al. (2012), Georgy et al. (2013), and Groh et al. (2019) use $\alpha_{\rm MLT} = \alpha^{\odot}_{\rm MLT} = 1.6467$ for massive star models, arguing that $\alpha_{\rm MLT}$ only changes to 1.6 for very high-mass stars, $M = 150 M_{\odot}$ (Georgy et al. 2013). This variation was found by accounting for the differences in the massive stars equation of state.

However, 3D simulations of convection in low-mass stars have shown that there is a strong $\alpha_{\rm MLT}$ dependence on $T_{\rm eff}$ and log g (e.g. Trampedach et al. (2014), where for $T_{\rm eff} < 5000$ K a $\alpha_{\rm MLT} > 1.8$ is found). Work by Magic, Weiss & Asplund (2015) also finds a difference of ~ 20 per cent in the $\alpha_{\rm MLT}$ depending on the mass of the star. Although these studies do not extend to the parameter ranges relevant for RSGs, they point out that the value of $\alpha_{\rm MLT}$ is not independent of the mass.

Specifically studying RSGs, Chun et al. (2018) adopts the approach of tuning $\alpha_{\rm MLT}$ to match the locations of RSGs in a range of metallicity environments. Regardless of which RSG temperature scales are used, they argue for a metallicity-dependent $\alpha_{\rm MLT}$. Moreover, Dessart et al. (2013) studies the supernova type II-P (SN IIP) progenitors, varying the parameters (e.g. mixing length, overshoot, rotation, metallicity) in the stellar evolution code MESA

STAR. They find that the RSG radii should be reduced in comparison with Levesque et al. (2005), implying that the $T_{\rm eff}$ of RSGs should be higher than the Levesque et al. (2005) temperature scale.

The previously described work, in combination with our results presented in this study, are part of a growing body of evidence that the assumption of a solar mixing length parameter is not adequate to explain the locations of RSGs in the HRD as a function of metallicity.

6 CONCLUSIONS

We have analysed a total of 28 RSGs observed with VLT-XSHOOTER from the neighbouring galaxies LMC, SMC, and WLM, by fitting the flux of the SED regions free from molecular features. Our main conclusions are as follows:

(i) We find an average RSG $T_{\rm eff}$ for WLM which is ∼300 K warmer than that in either of the MCs. This trend of increasing average $T_{\rm eff}$ with decreasing Z is in qualitative agreement with theoretical predictions.

(ii) From population synthesis analysis, we find that there is a systematic offset between expected and observed temperatures of RSGs at all metallicities. Specifically, RSGs in evolutionary models are too cool by ∼200 K. This could be due to a wrong estimation of the mixing length parameter for 1D models of massive stars.

ACKNOWLEDGEMENTS

We would like to thank the referee for useful comments that helped improve the paper. GGT is supported by a scholarship from the Liverpool John Moores University. GGT wants to thank the useful comments from Ricardo Schiavon, Sarah McDonald, and Sylvia Ekström. RPK acknowledges support by the Munich Excellence Cluster Origins funded by the Deutsche Forschungsgemeinschaft (DFG, German Research Foundation) under Germany's Excellence Strategy EXC-2094 390783311.

DATA AVAILABILITY

The data underlying this article will be shared on reasonable request to the corresponding author. The data sets were derived from sources in the public domain: http://archive.eso.org/cms.html.

REFERENCES

Avni Y., 1976, ApJ, 210, 642
Beasor E. R., Davies B., Smith N., Gehrz R. D., Figer D. F., 2021, ApJ, 912, 16
Bergemann M., Kudritzki R.-P., Würl M., Plez B., Davies B., Gazak Z., 2013, ApJ, 764, 115
Böhm-Vitense E., 1958, Z. Astrophys., 46, 108
Boyer M. L. et al., 2015, ApJS, 216, 10
Cardelli J. A., Clayton G. C., Mathis J. S., 1989, ApJ, 345, 245
Chambers K. C. et al., 2016, preprint (arXiv:1612.05560)
Chun S.-H., Yoon S.-C., Jung M.-K., Kim D. U., Kim J., 2018, ApJ, 853, 79
D'Odorico S. et al., 2006, in McLean I. S., Iye M., eds, SPIE Conf. Ser. Vol. 6269, X-shooter UV- to K-band Intermediate-Resolution High-Efficiency Spectrograph for the Vlt: Status Report at the Final Design Review. SPIE, Bellingham, p. 626933
Davies B., Beasor E. R., 2020, MNRAS, 493, 468
Davies B. et al., 2013, ApJ, 767, 3
Davies B., Kudritzki R.-P., Gazak Z., Plez B., Bergemann M., Evans C., Patrick L., 2015, ApJ, 806, 21
Davies B. et al., 2017, ApJ, 847, 112
Davies B., Crowther P. A., Beasor E. R., 2018, MNRAS, 478, 3138
Dessart L., Hillier D. J., Waldman R., Livne E., 2013, MNRAS, 433, 1745
Dorda R., Negueruela I., González-Fernández C., Tabernero H. M., 2016, A&A, 592, A16
Ekström S. et al., 2012, A&A, 537, A146
Gaia Collaboration, 2018, A&A, 616, A1
Georgy C. et al., 2013, A&A, 558, A103
González-Fernández C., Dorda R., Negueruela I., Marco A., 2015, A&A, 578, A3
Gordon K. D., Clayton G. C., Misselt K. A., Land olt A. U., Wolff M. J., 2003, ApJ, 594, 279
Groh J. H. et al., 2019, A&A, 627, A24
Gustafsson B., Edvardsson B., Eriksson K., Jørgensen U. G., Nordlund Å.,Plez B., 2008, A&A, 486, 951
Hayashi C., Hoshi R., 1961, PASJ, 13, 442
Levesque E. M., Massey P., 2012, AJ, 144, 2
Levesque E. M., Massey P., Olsen K. A. G., Plez B., Josselin E., Maeder A., Meynet G., 2005, ApJ, 628, 973
Levesque E. M., Massey P., Olsen K. A. G., Plez B., Meynet G., Maeder A., 2006, ApJ, 645, 1102
McConnachie A. W., Irwin M. J., Ferguson A. M. N., Ibata R. A., Lewis G. F., Tanvir N., 2005, MNRAS, 356, 979
McMahon R. G., Banerji M., Gonzalez E., Koposov S. E., Bejar V. J., Lodieu N., Rebolo R., VHS Collaboration, 2013, The Messenger, 154, 35
Maeder A., Meynet G., 2001, A&A, 373, 555
Magic Z., Weiss A., Asplund M., 2015, A&A, 573, A89
Meynet G., Maeder A., 2000, A&A, 361, 101
Meynet G., Maeder A., 2002, A&A, 390, 561
Pickles A., Depagne É., 2010, PASP, 122, 1437
Schlafly E., Green G., Finkbeiner D. P., Rix H., 2014, Am. Astron. Soc. Meeting Abstr. 223, 116.04
Tabernero H. M., Dorda R., Negueruela I., González-Fernández C., 2018, MNRAS, 476, 3106
Trampedach R., Stein R. F., Christensen-Dalsgaard J., Nordlund Å.,Asplund M., 2014, MNRAS, 445, 4366
Urbaneja M. A., Kudritzki R.-P., Bresolin F., Przybilla N., Gieren W., Pietrzyński G., 2008, ApJ, 684, 118
Wenger M. et al., 2000, A&AS, 143, 9
Wolf C. et al., 2018, Publ. Astron. Soc. Aust., 35, e010

APPENDIX A: ANALYSIS OF RSGS

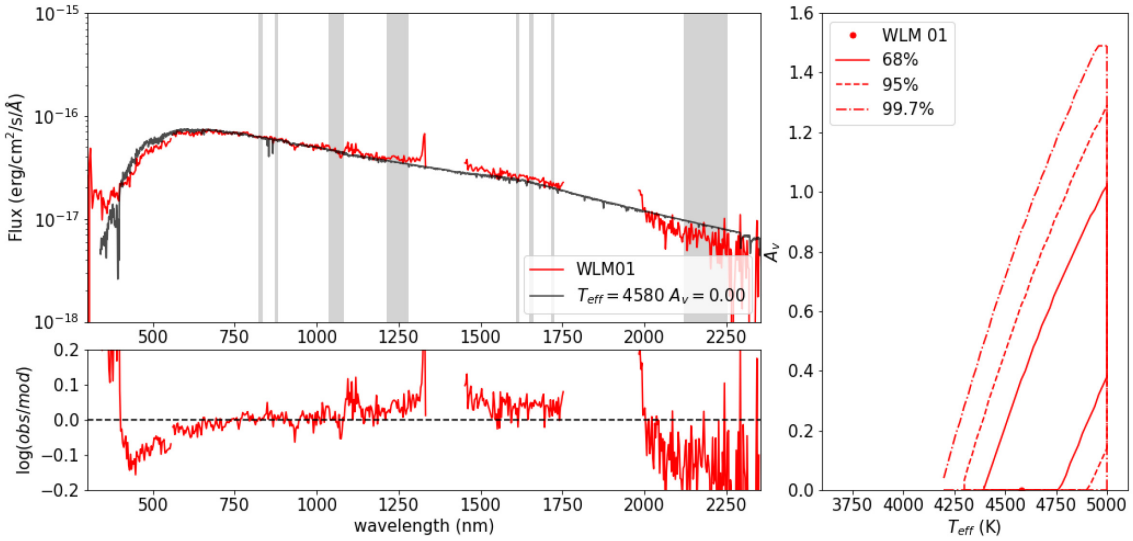

Figure A1. Three panels showing the results of the analysis for WLM 01. *Upper left:* Shows the smoothed data (red) and best-fitting MARCS model (black), while the SED regions for the analysis are shown in grey. *Lower left:* The residuals of the fit. *Right:* shows the 68 per cent, 95 per cent, and 99.7 per cent confidence contours for the best-fitting effective temperature and extinction.

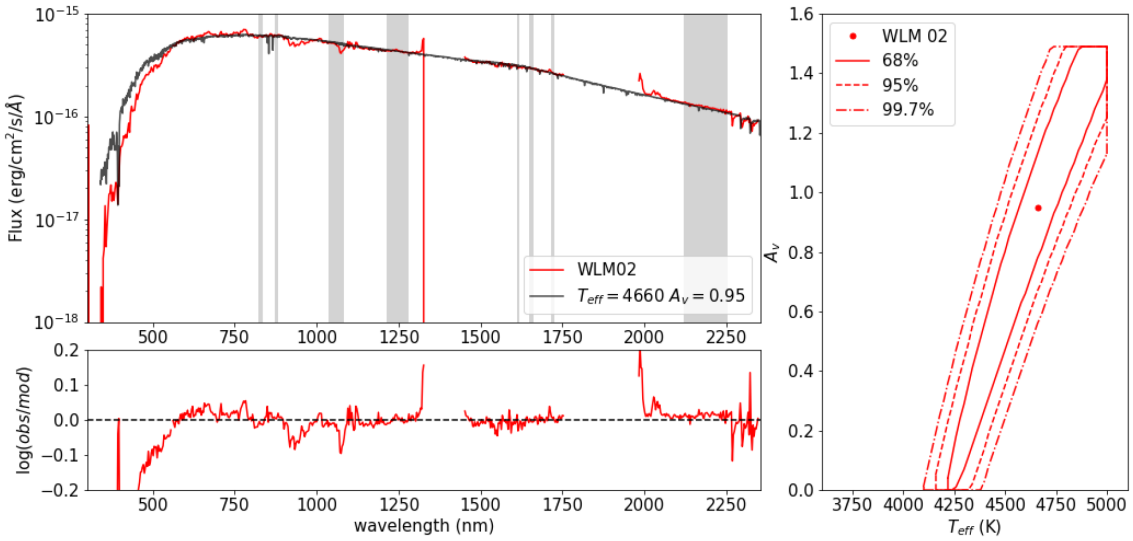

Figure A2. Same as Fig. A1 but for WLM 02.

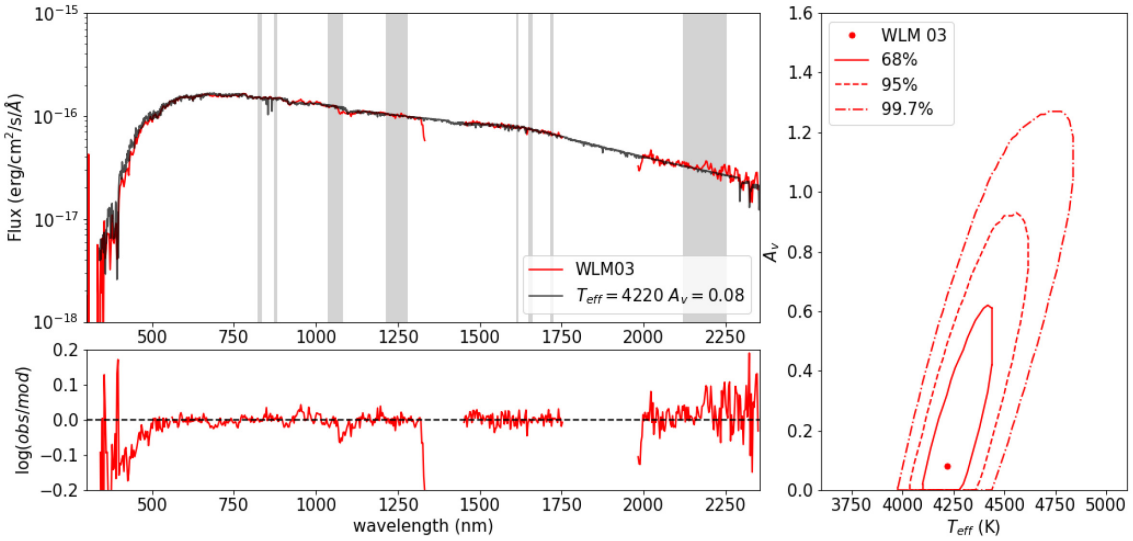

Figure A3. Same as Fig. A1 but for WLM 03.

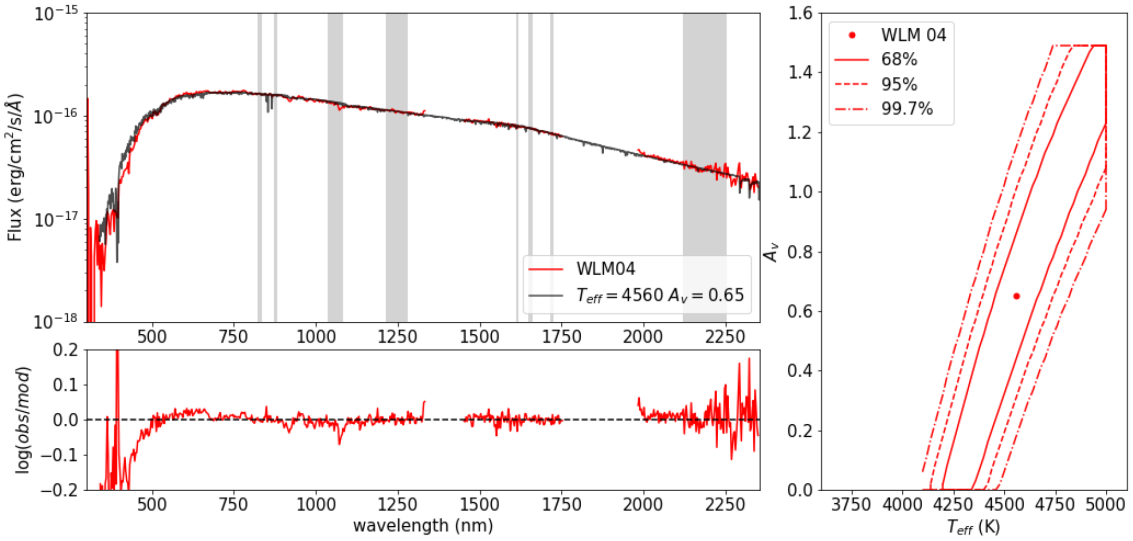

Figure A4. Same as Fig. A1 but for WLM 04.

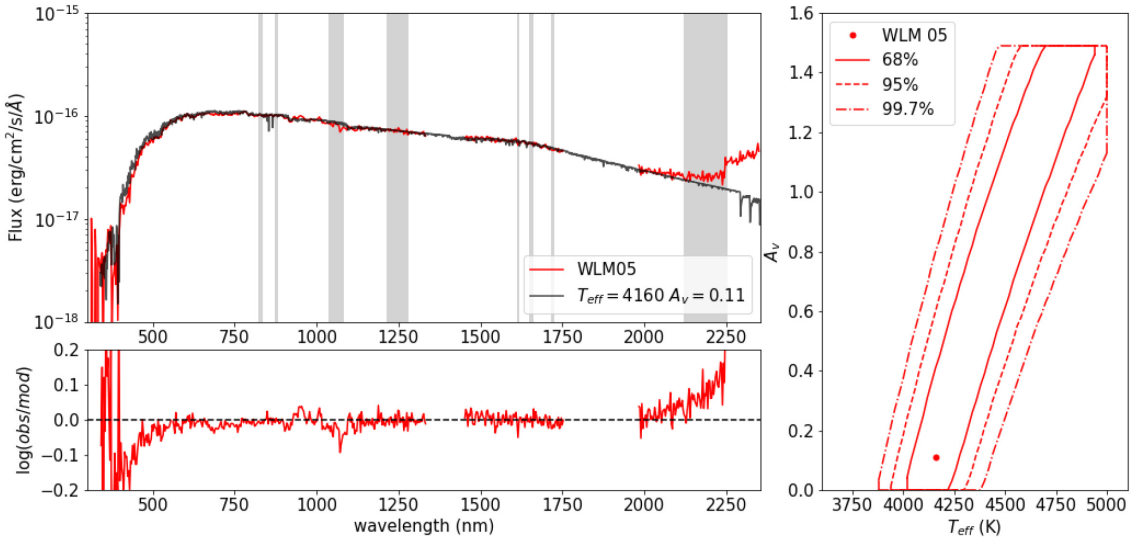

Figure A5. Same as Fig. A1 but for WLM 05.

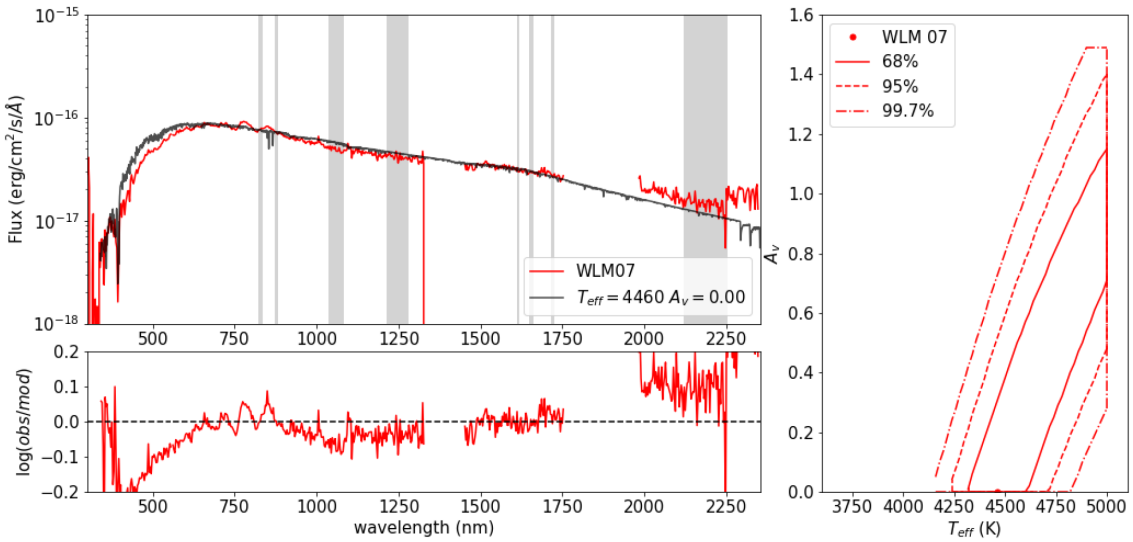

Figure A6. Same as Fig. A1 but for WLM 07. This star is the problematic case, and we suspect it is not part of the galaxy WLM.

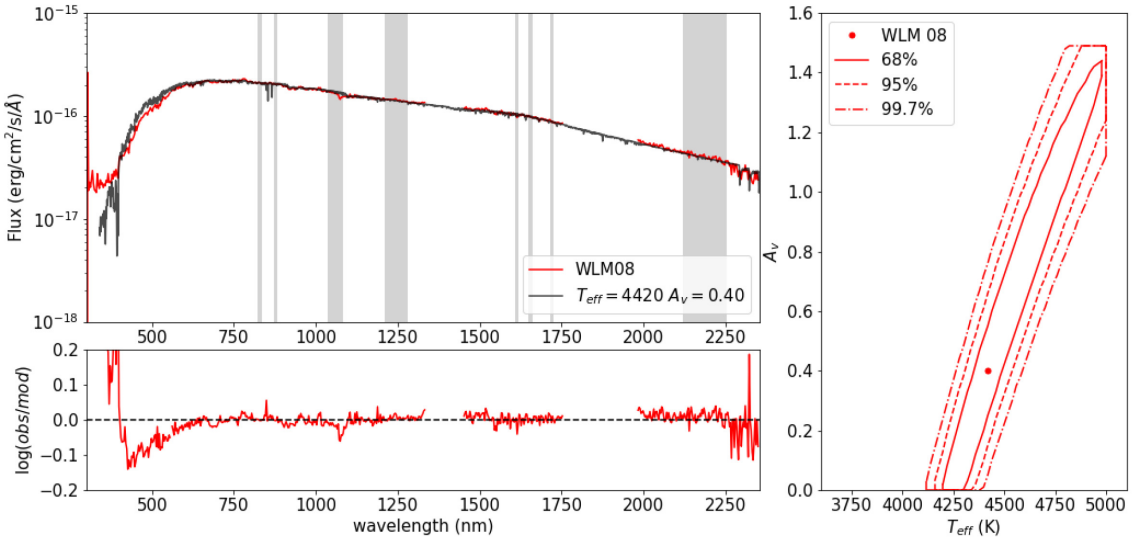

Figure A7. Same as Fig. A1 but for WLM 08.

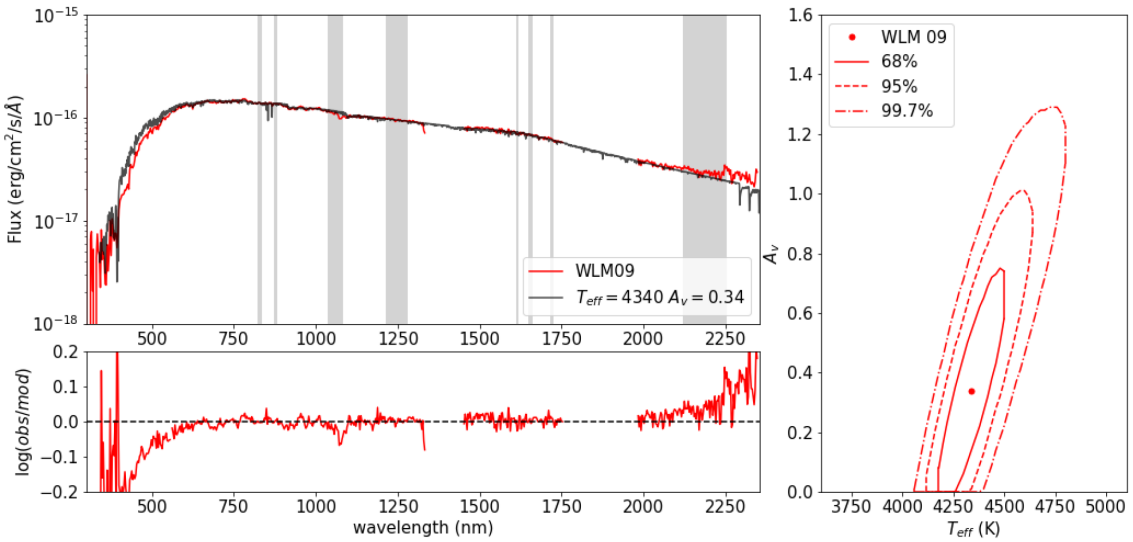

Figure A8. Same as Fig. A1 but for WLM 09.

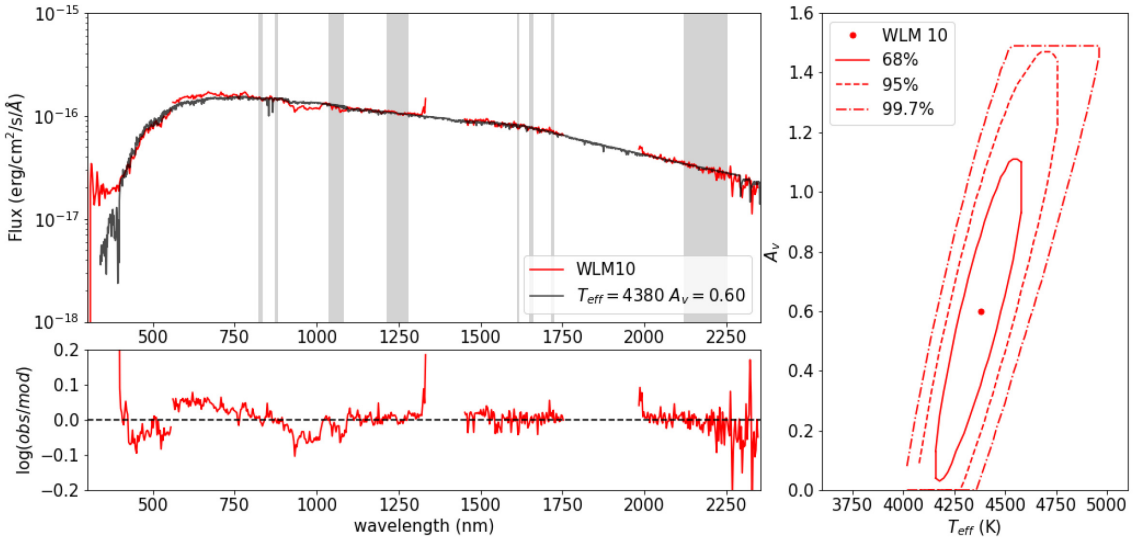

Figure A9. Same as Fig. A1 but for WLM 10.

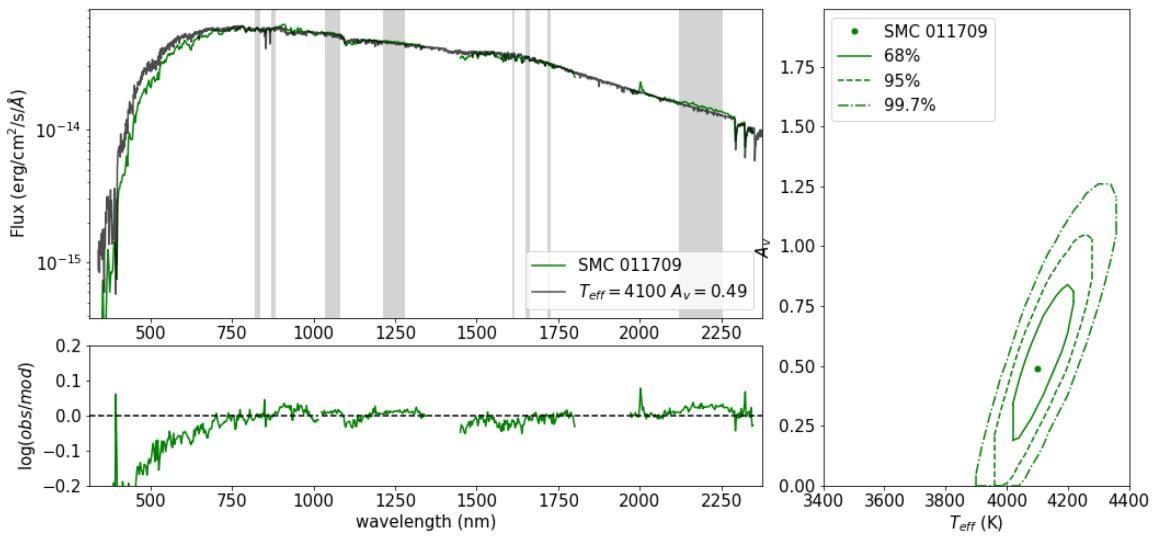

Figure A10. Three panels showing the results of the analysis for the SMC 011709. *Upper left:* Shows the smoothed data (green) and best-fitting MARCS model (black), while the SED regions for the analysis are shown in grey. *Lower left:* The residuals of the fit. *Right:* shows the 68 per cent, 95 per cent, and 99.7 per cent confidence contours for the best-fitting effective temperature and extinction.

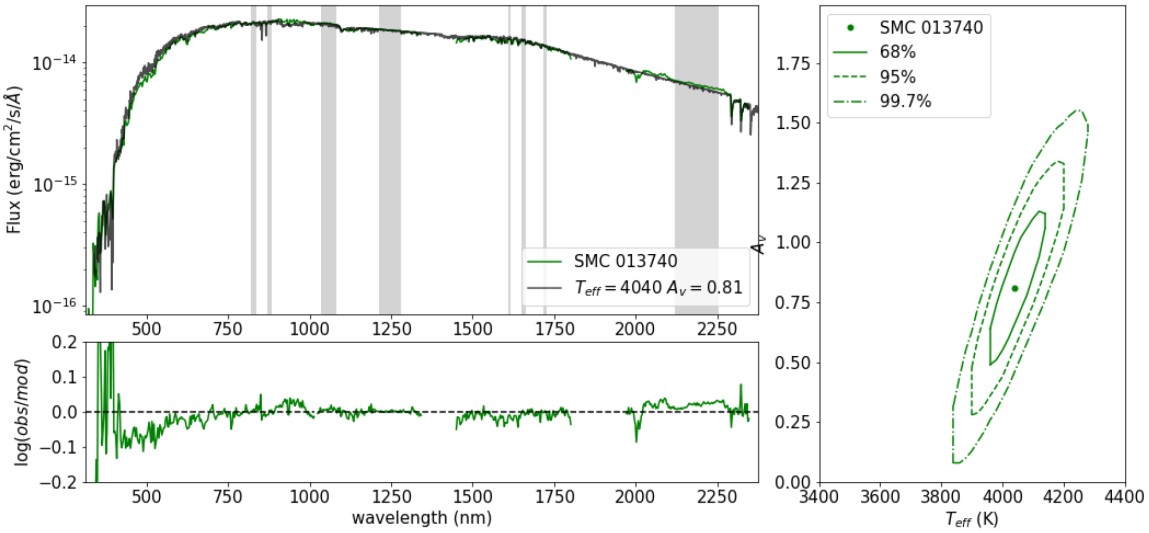

Figure A11. Same as Fig. A10 but for SMC 013740.

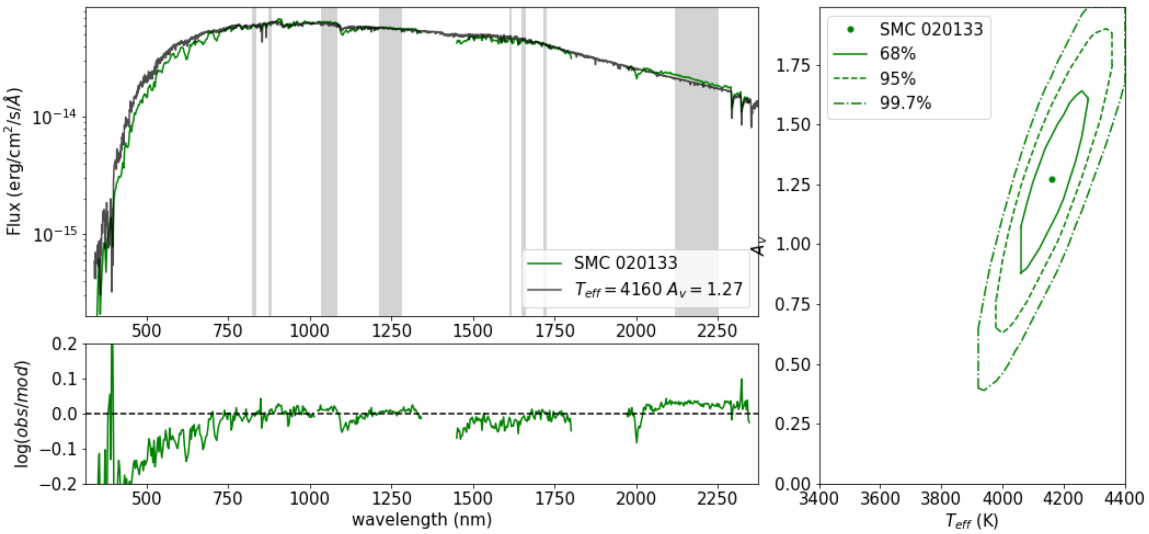

Figure A12. Same as Fig. A10 but for SMC 020133.

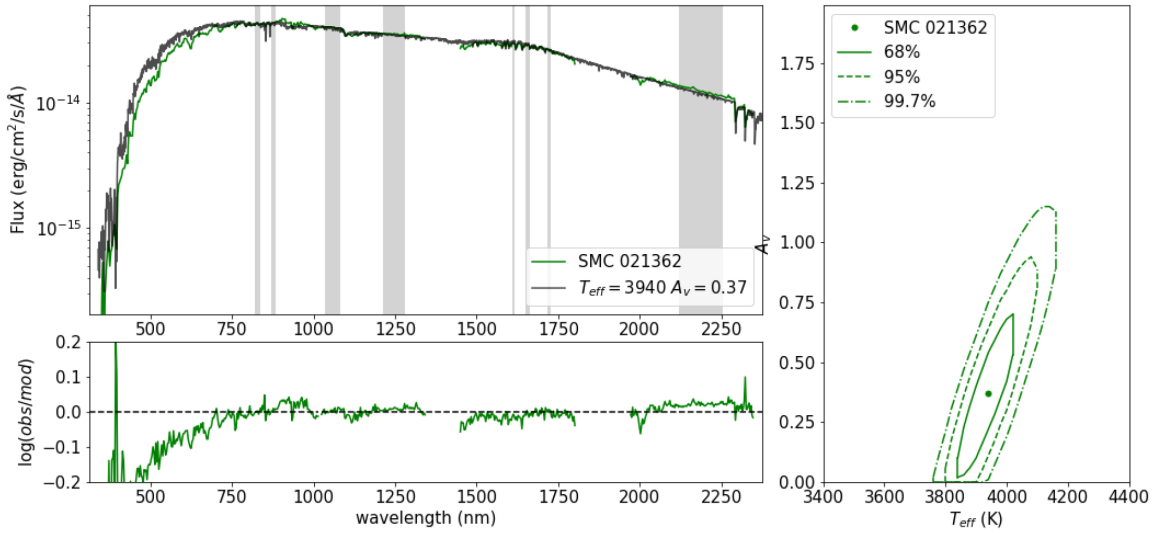

Figure A13. Same as Fig. A10 but for SMC 021362.

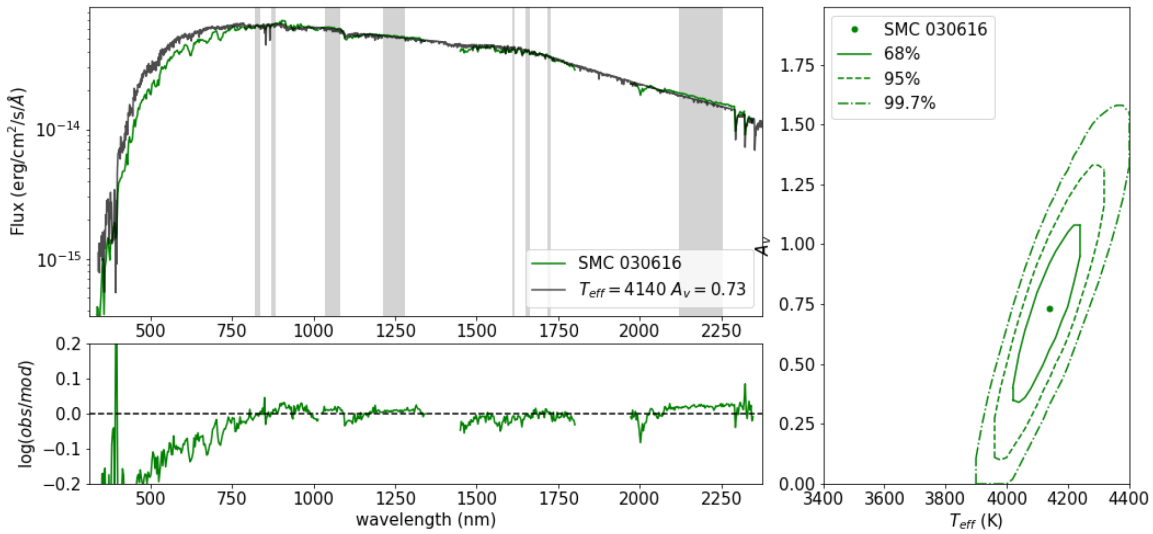

Figure A14. Same as Fig. A10 but for SMC 030616.

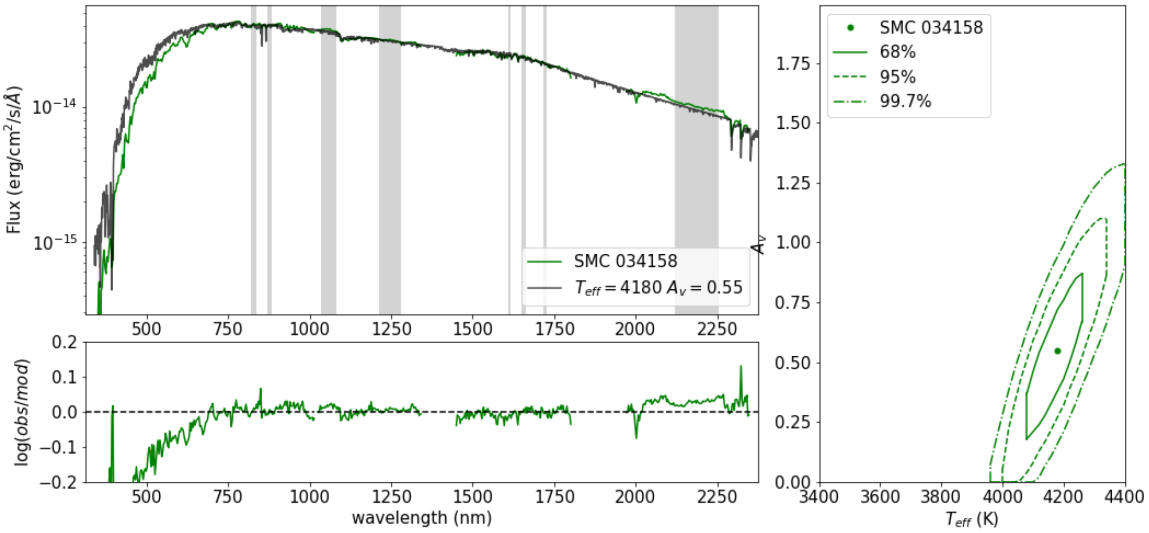

Figure A15. Same as Fig. A10 but for SMC 034158.

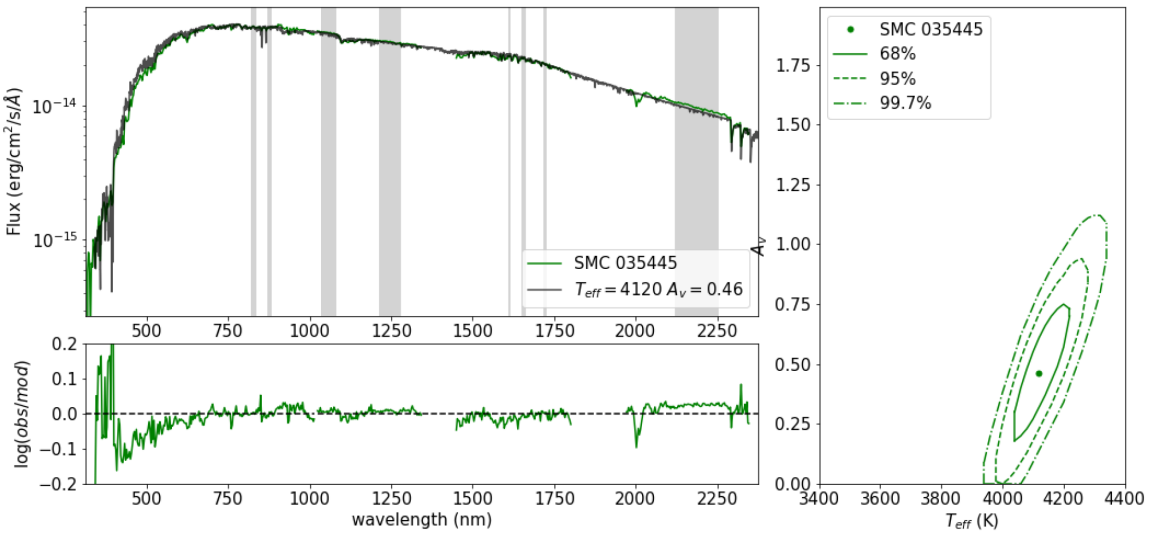

Figure A16. Same as Fig. A10 but for SMC 035445.

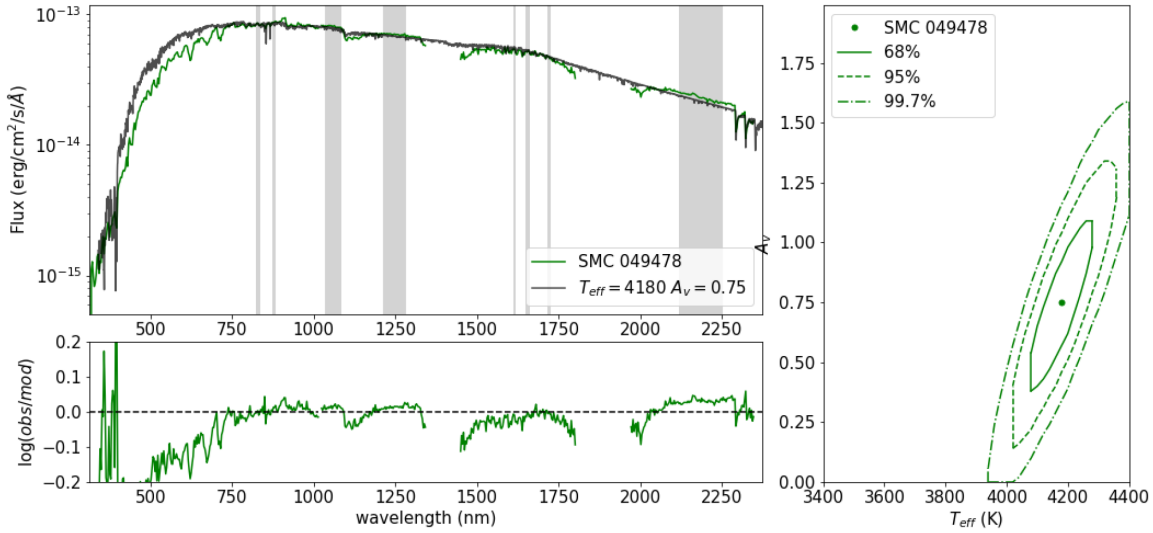

Figure A17. Same as Fig. A10 but for SMC 049478.

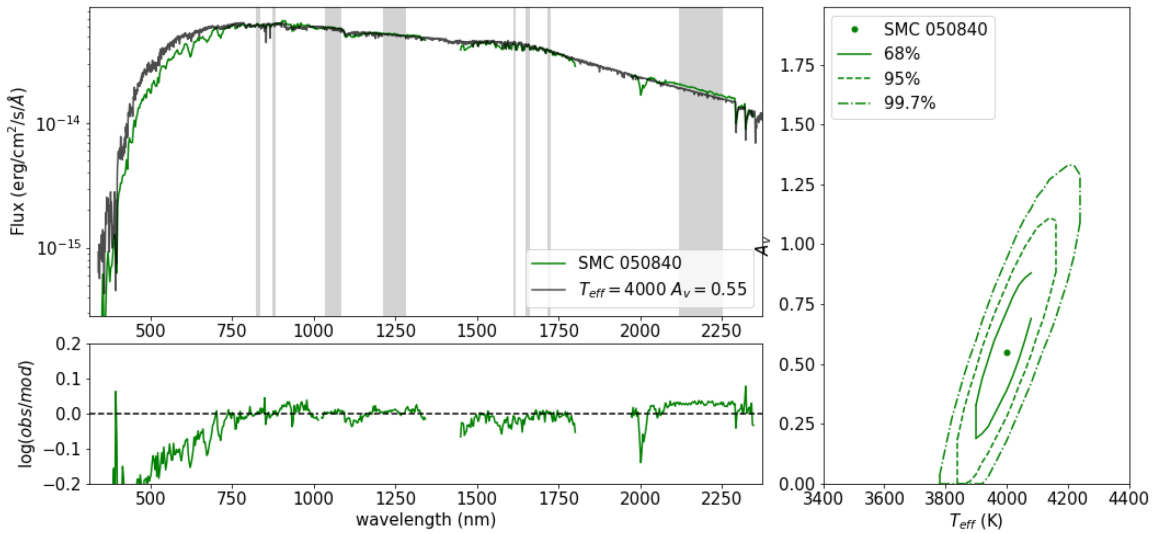

Figure A18. Same as Fig. A10 but for SMC 050840.

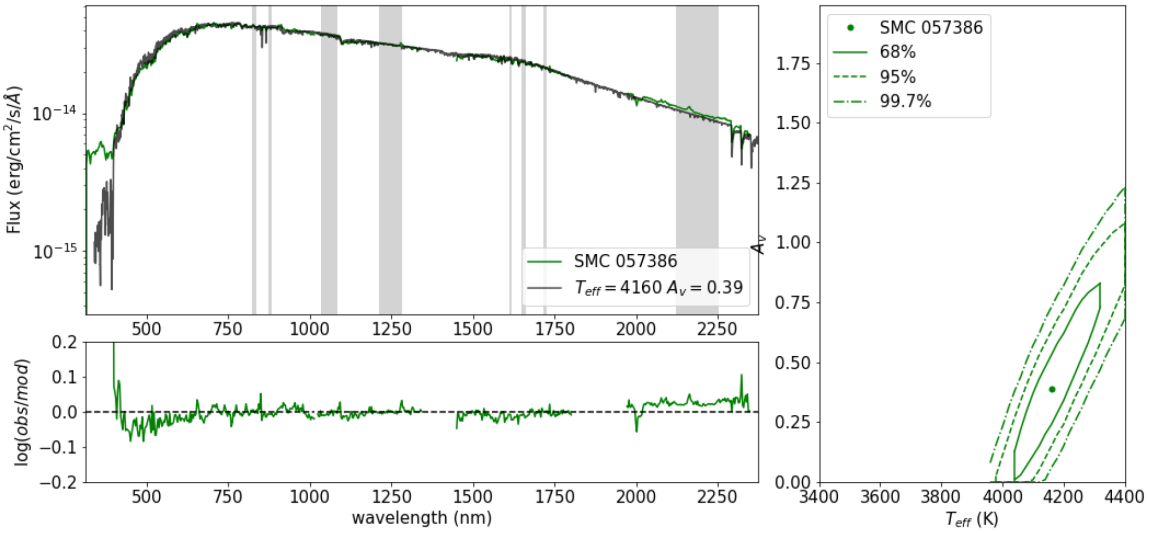

Figure A19. Same as Fig. A10 but for SMC 057386.

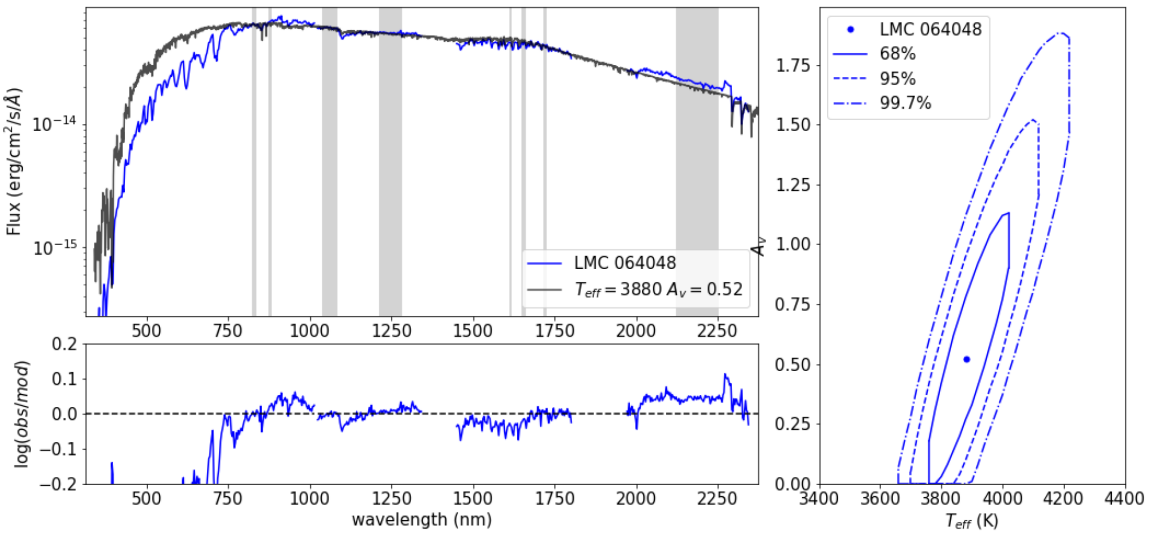

Figure A20. Three panels showing the results of the analysis at the LMC 064048. *Upper left:* Shows the smoothed data (blue) and best-fitting MARCS model (black), while the SED regions for the analysis are shown in grey. *Lower left:* The residuals of the fit. *Right:* shows the 68 per cent, 95 per cent, and 99.7 per cent confidence contours for the best-fitting effective temperature and extinction.

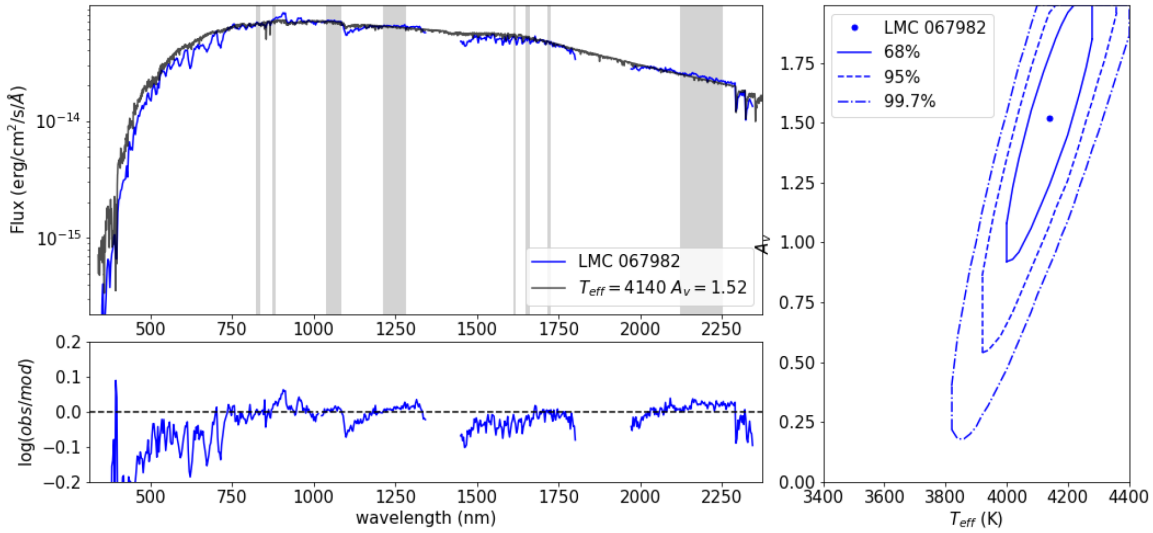

Figure A21. Same as Fig. A20 but for LMC 067982.

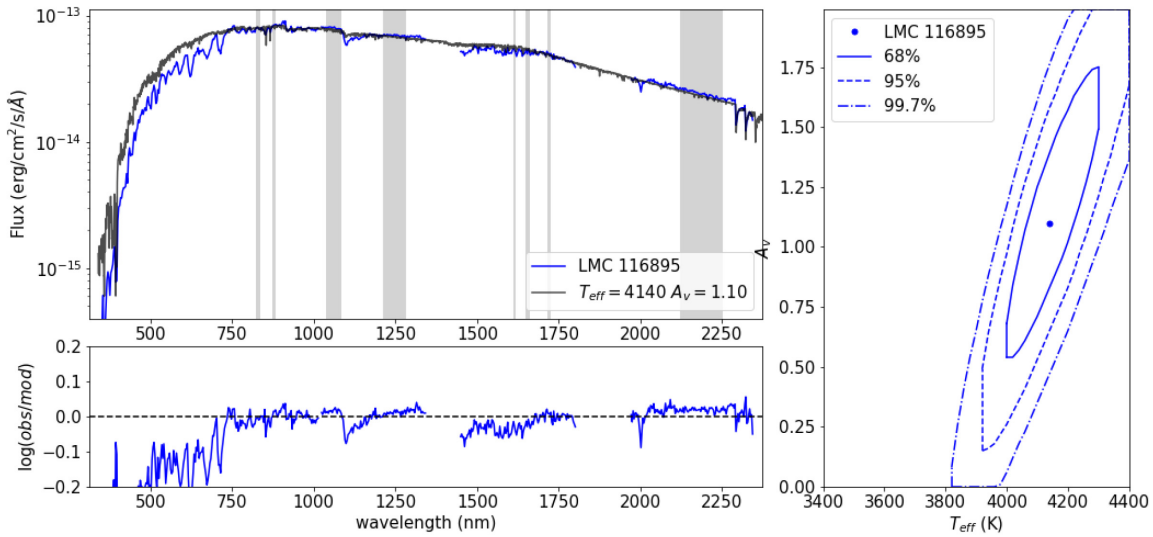

Figure A22. Same as Fig. A20 but for LMC 116895.

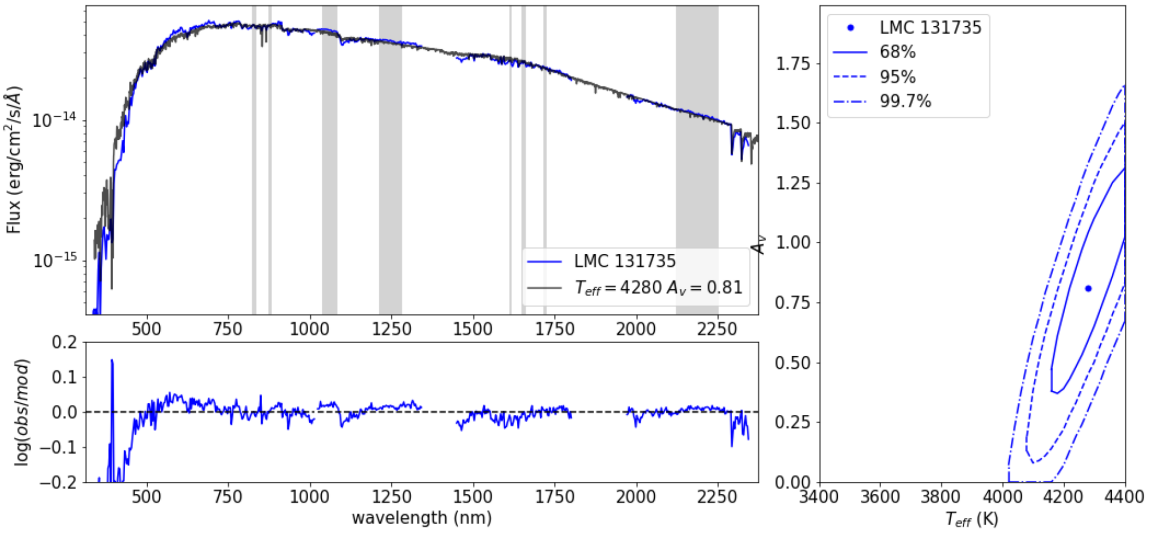

Figure A23. Same as Fig. A20 but for LMC 131735.

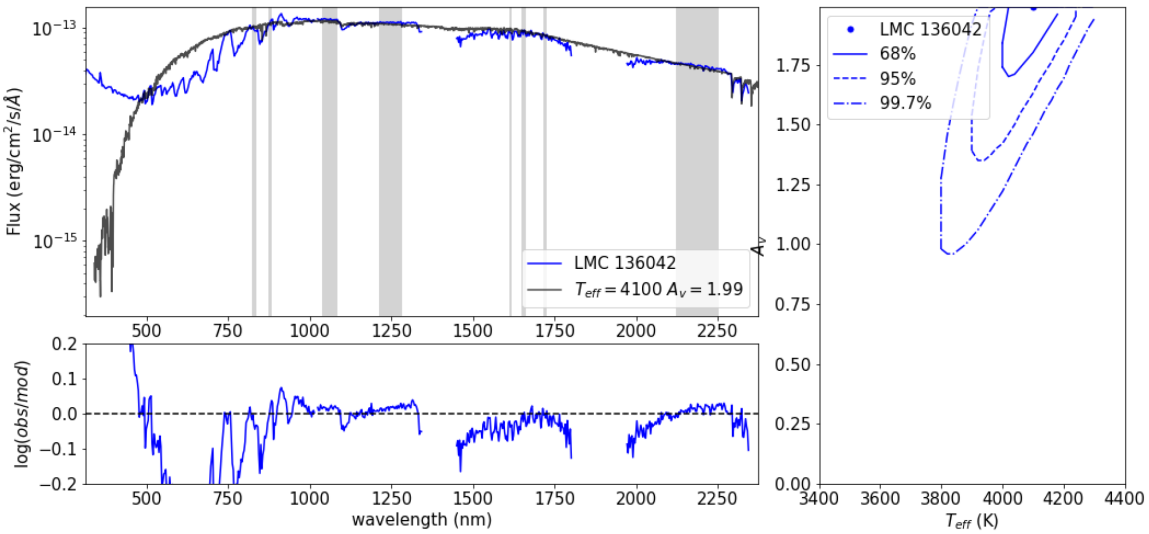

Figure A24. Same as Fig. A20 but for LMC 136042. This is a problematic case that can have a near blue star that contaminates the spectrum.

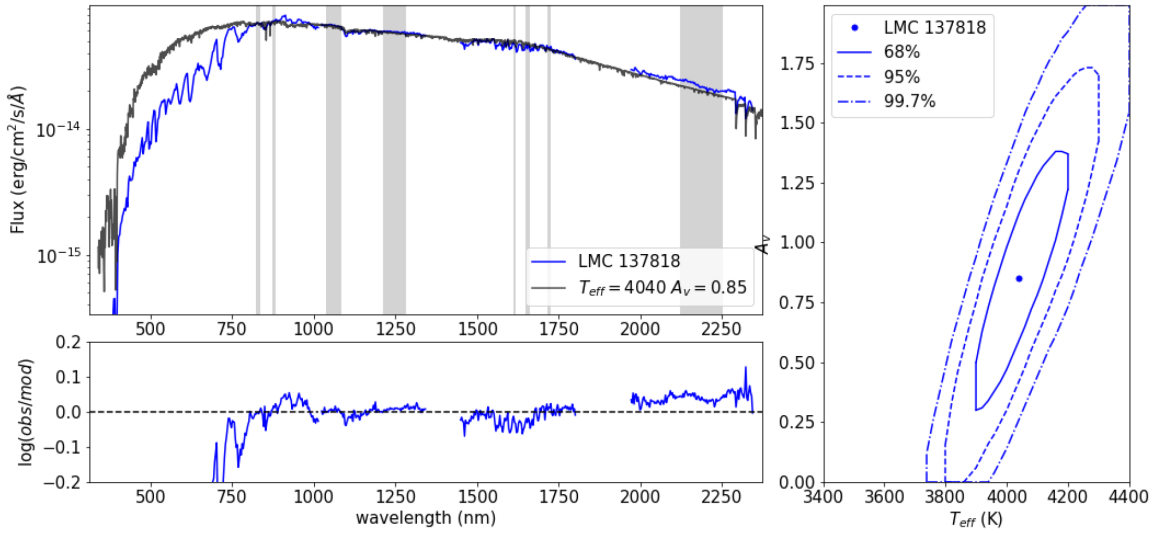

Figure A25. Same as Fig. A20 but for LMC 137818.

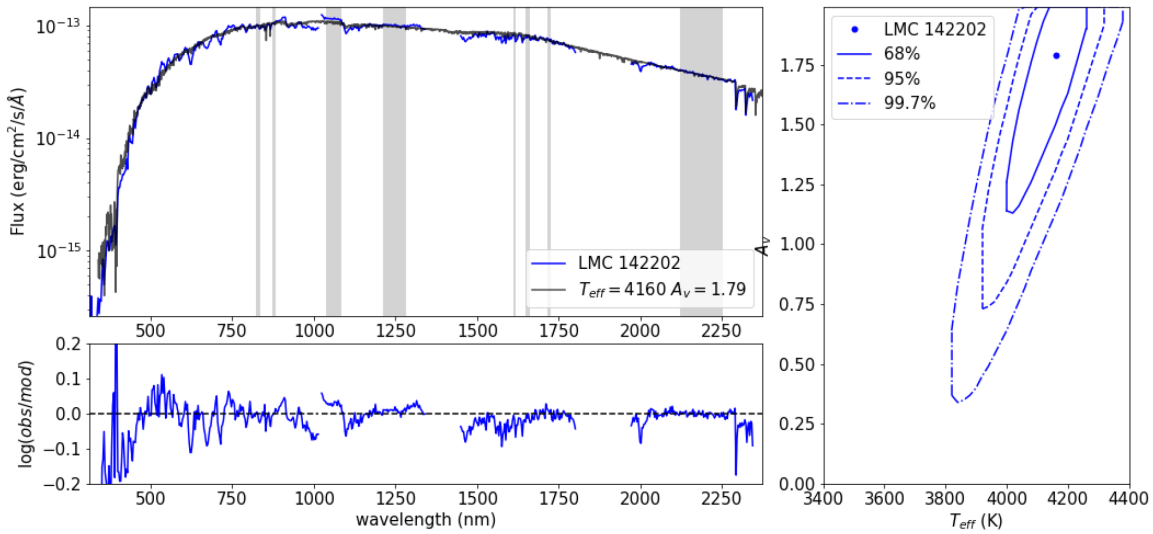

Figure A26. Same as Fig. A20 but for LMC 142202.

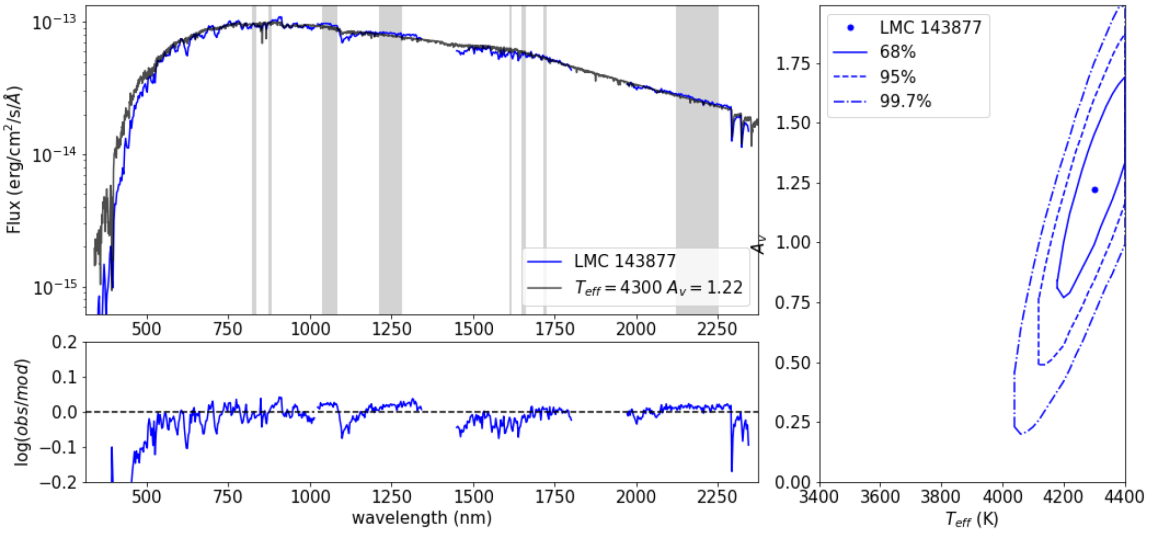

Figure A27. Same as Fig. A20 but for LMC 143877.

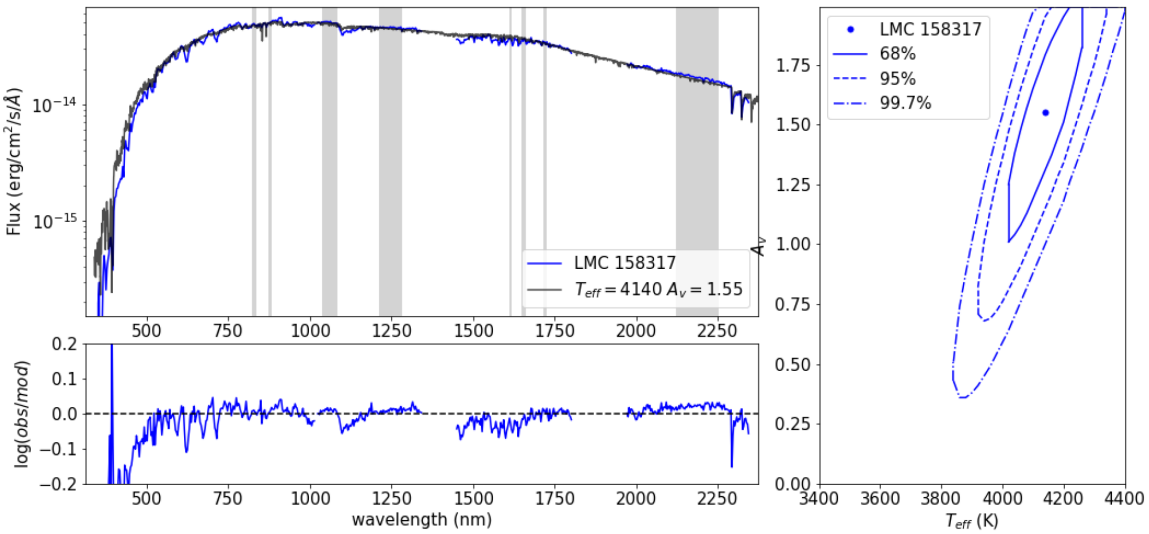

Figure A28. Same as Fig. A20 but for LMC 158317.

This paper has been typeset from a TEX/LATEX file prepared by the author.